Progress in Oceanography 206 (2022) 102829

Contents lists available at ScienceDirect

Progress in Oceanography

journal homepage: www.elsevier.com/locate/pocean

# Characterization of intraseasonal fluctuations in the abyssal South China Sea: An insight into the energy pathway

Qi Quan[a,b], Zhiqiang Liu[b,*], Yang Yang[c], Zhongya Cai[d,e], Han Zhang[f,g], Xiaohui Liu[f]

[a] State Key Laboratory of Estuarine and Coastal Research, East China Normal University, Shanghai, China
[b] Department of Ocean Science and Engineering, Southern University of Science and Technology, Shenzhen, China
[c] School of Marine Sciences, Nanjing University of Information Science and Technology, Nanjing, China
[d] State Key Laboratory of Internet of Things for Smart City and Department of Civil and Environmental Engineering, University of Macau, Macau
[e] Center for Ocean Research in Hongkong and Macau, Macau
[f] State Key Laboratory of Satellite Ocean Environment Dynamics, Second Institute of Oceanography, Ministry of Natural Resources, Hangzhou, China
[g] Shanghai Typhoon Institute, China Meteorological Administration, Shanghai, China

ARTICLE INFO

*Keywords:*
Intraseasonal fluctuations
Abyssal ocean
South China Sea
Energetics

ABSTRACT

Energetics of the abyssal ocean account greatly for the redistribution and dissipation of global oceanic energy. In this study, we characterize the intraseasonal fluctuations in the deep South China Sea (SCS) and evaluate the relevant energy budget using observations and numerical simulations. The results indicate substantial geographical inhomogeneity in the intraseasonal energy reservoir. The high-energy zones are located in the northwest of the Luzon Strait, northern slopes, deep western boundary current region, and southwestern cyclonic gyre region, where the intraseasonal fluctuations account for about 70% of the deep energy variability. Vorticity and divergence patterns of the intraseasonal motions are suggestive of quasigeostrophic dynamics, which are mostly attributed to the hybrid topographic–planetary Rossby waves. The flow field exhibits a weak lateral shear and appears to have symmetric instability with negative vorticity skewness, particularly over the sloping topography. Energetics analysis demonstrates that the intraseasonal fluctuations in the abyssal SCS obtain energy primarily from the upper layer through pressure work, while secondarily from advective transport and cross-scale transfer due to instability of the deep circulation. To reach equilibrium, the energy gained is mostly damped by dissipations. As another reference in the marginal sea with intensive mixing, our study highlights the potential universality in how the intraseasonal energy is fueled and dissipated in the abyss.

## 1. Introduction

Redistribution and dissipation of energy in the deep ocean has been suggested to be critical to the global energy budget (e.g., Wunsch & Ferrari, 2004). Here, we focus on the largest marginal sea in the northwestern Pacific Ocean, the South China Sea (SCS), where the topography-enhanced diapycnal mixing is observed to be two orders of magnitude stronger than the open ocean (Tian et al., 2009), and provide an overview of the abyssal intraseasonal fluctuations in this region by teasing apart the relevant energetics for the first time (as far as the authors are aware).

Significant intraseasonal fluctuations of the deep flow over steep topography have been observed in oceans worldwide, such as along the mainstream of the Gulf Stream, in the Gulf of Mexico, and in the Artic Ocean's Beaufort Gyre (Thompson & Luyten, 1976; Thompson, 1977; Hogg, 1981, 2000; Johns & Watts, 1986; Pickart & Watts, 1990; Hamilton, 1990, 2007; Peña-Molino et al., 2012; Zhao & Timmermans, 2018). These fluctuations, with periods of several to hundreds of days, contribute greatly to the total variability in the deep flow (e.g., 80%–90% in the Gulf of Mexico; Hamilton, 2009), which is particularly critical in the choke point of the meridional overturning circulation, affecting the mass and heat transport in the global ocean (e.g., Ma et al., 2019). Existing studies have attributed the energy sources of these intraseasonal fluctuations in the deep oceans to 1) intra-scale input from the mesoscale perturbations in the upper layer through potential vorticity (PV) adjustments in response to the changing depths of the bottom and the interface between layers, for example, the periodic Gulf Stream meanders propagating eastward (Pickart, 1995); and 2) inter-scale input from large-scale circulation due to instabilities, for example, the available potential energy (APE) released through

---

* Corresponding author.
*E-mail address:* liuzq@sustech.edu.cn (Z. Liu).

https://doi.org/10.1016/j.pocean.2022.102829
Received 6 September 2021; Received in revised form 17 May 2022; Accepted 26 May 2022
Available online 1 June 2022

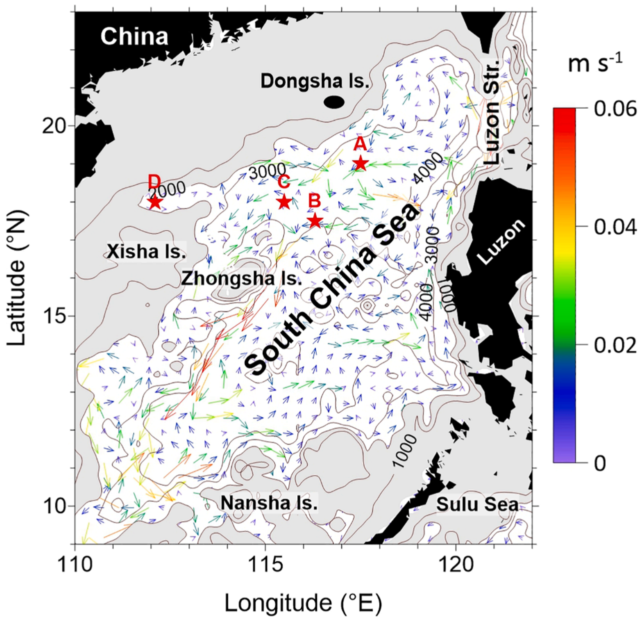

**Fig. 1.** Abyssal SCS circulation (m s$^{-1}$) averaged from 2000 m to the bottom based on HYCOM GLBv0.08. Contours represent the isobaths (m). Note that the areas shallower than 2000 m are masked. The red stars denote the mooring sites A-D. Modified from Quan et al. (2021a).

baroclinic instability of the Loop Current in the Gulf of Mexico (Oey, 2008; Xu et al., 2013; Donohue et al., 2016; Hamilton et al., 2019). In fact, the relative importance of these two energy sources is spatially and temporally dependent.

The abyssal SCS is enclosed below 2000 m and featured by a basin-scale cyclonic circulation involving subbasin gyres (Fig. 1; Wang et al., 2011; Lan et al., 2013; D. Wang et al., 2016). Similar to the Gulf of Mexico, energetic intraseasonal fluctuations of deep flow have also been observed in the SCS. Based on 5-yr observations near the Nansha Islands, Shu et al. (2016) found persistent fluctuations of 9–14 days in the southern SCS, with the resulting current being comparable to the tidal current that is one order of magnitude larger than the ambient deep flow. Southeast of the Zhongsha Islands, the temporal variability of the deep western boundary current (DWBC) was found to be dominated by 90-day fluctuations propagating westward (Zhou et al., 2017). Over the slope southeast of the Dongsha Islands, the fluctuations with peak spectral energy at approximately 14.5 days were found to contribute more than 40% of the total bottom-flow variability (Wang et al., 2019). With an intensive mixing effect, these intraseasonal fluctuations play a potential role in regulating abyssal circulation that is analogous to tides (Quan & Xue, 2019). However, the available observations are too limited to characterize basin-wide intraseasonal motions in the deep SCS.

Based on the vertical coherence between layers, previous studies have largely attributed the energy sources of the intraseasonal fluctuations in the deep SCS to the mesoscale eddies in the upper layer (Shu et al., 2016; Wang et al., 2019; Zheng et al., 2021). Nevertheless, the mechanism by which the surface eddy kinetic energy (KE) is injected into the deep SCS is not well understood. Moreover, the abyssal intraseasonal variability is also suggested to be forced by the Luzon overflow or the related deep eddies (Zhou et al., 2020). Unfortunately, how the energy is transferred from the background flow to the fluctuations is not clear. Recently, Quan et al. (2021a, b) systematically depicted topographic Rossby waves (TRWs; with periods of 5–60 days) in the deep SCS and pointed out that the Kuroshio intrusion and the related eddies serve as the major energy source for these subinertial waves through pressure work. These pilot works focusing on the specific phenomena show a reference for how intraseasonal fluctuations in the abyssal SCS drain energy from the surroundings. However, the energetics for the entire intraseasonal regime in the deep SCS and the relative importance of different mechanisms remain unsolved.

**Table 1**
Deep moorings deployed in this study.

| Site | Location | Water depth | Measurement period | Instrument | Sampling interval |
|---|---|---|---|---|---|
| A | 117.5°E, 19°N | 3690 m | 06/11/14–03/29/15 | Seaguard at 100 m above the bottom | 10 min |
| B | 116.3°E, 17.5°N | 3990 m | 06/11/14–03/29/15 | | |
| C | 115.5°E, 18°N | 3840 m | 06/11/14–03/29/15 | | |
| D | 112.1°E, 18°N | 2500 m | 08/07/16–10/26/16 | | |

In this study, we attempt to answer these questions by employing observations and numerical simulations with a recently developed multiscale energy analysis and canonical transfer theory. The remainder of this paper is organized as follows. The data and methods are described in Section 2. Section 3 presents the energy reservoirs, dynamics, and instability of the intraseasonal fluctuations in the deep SCS. The underlying energetics are discussed in Section 4. Finally, Section 5 summarizes the study.

## 2. Data and methods

### 2.1. Data

Here we use four moorings to reveal the deep flow variability and evaluate the numerical simulations. All the mooring sites were located in the northern SCS (red stars in Fig. 1), and the details are listed in Table 1. A Seaguard current meter was employed at 100 m above the bottom of each site, with a sampling interval of 10 min. Velocity was continuously recorded for approximately 9 months from June 11, 2014 to March 29, 2015 at sites A-C and 3 months from August 7, 2016 to October 26, 2016 at site D. The percentage of valid data was higher than 95%. Note that variability at a time scale longer than 30 days may not be resolved at site D due to a short measurement period.

Because of the very limited spatiotemporal coverage of the observations, the outputs of the Hybrid Coordinate Ocean Model (HYCOM) + Navy Coupled Ocean Data Assimilation global 1/12° Analysis (GLBv0.08; Cummings, 2005; Cummings & Smedstad, 2013) from 2013 to 2018 are also used to pursue this study. The 3-hourly data have a horizontal resolution of approximately 8.4–9.2 km in the SCS and 41 vertical levels from 0 to 5500 m. This dataset has been widely employed to study the multiscale processes in the SCS (e.g., Shu et al., 2014; Zhang et al., 2017; Yan et al., 2019; Sun et al., 2020) and its validity in reproducing the abyssal intraseasonal fluctuations (e.g., TRWs) has already been evaluated against observations in our recent studies (Quan et al., 2021a, b), as well as in Section 3.1.

Note that the present model excludes the tidal forcing that contributes greatly to the abyssal mixing in the SCS (X. Wang et al., 2016). This could lead to discrepancies in the simulation but would not qualitatively change the dynamics discussed in this study because of the distinctly different time scales. Moreover, the available observations for data assimilation are so limited in the SCS that the HYCOM reanalysis in this region is close to a free-running case (Cummings & Smedstad, 2013). Hence, the model is thought to be kinetically and dynamically consistent in the SCS, which is feasible for the energetics analysis in our study.

### 2.2. Multiscale energy and vorticity analysis in a three-window framework

To investigate the characteristics and energetics of intraseasonal fluctuations in the abyssal SCS, we employ a recently developed method

**Table 2**

Expression and physical meaning of each term in the KE and APE equations on window $\varpi$. The colon operator is defined such that, for two dyadic products $\mathbf{AB}$ and $\mathbf{CD}$,$(\mathbf{AB}):(\mathbf{CD}) = (\mathbf{A}\cdot\mathbf{C})(\mathbf{B}\cdot\mathbf{D})$.

| Term | Expression | Physical meaning |
|---|---|---|
| $K^{\varpi}$ | $\frac{1}{2}\widehat{\mathbf{v}}_h^{\sim\varpi}\cdot\widehat{\mathbf{v}}_h^{\sim\varpi}$ | KE on window $\varpi$; $\mathbf{v}$ is the velocity vector |
| $\Delta Q_K^{\varpi}$ | $-\nabla\cdot\left[\frac{1}{2}(\widehat{\mathbf{v}\mathbf{v}_h})^{\sim\varpi}\cdot\widehat{\mathbf{v}}_h^{\sim\varpi}\right]$ | KE transport on window $\varpi$ |
| $\Gamma_K^{\varpi}$ | $\frac{1}{2}[(\widehat{\mathbf{v}\mathbf{v}_h})^{\sim\varpi}:\nabla\widehat{\mathbf{v}}_h^{\sim\varpi} - \nabla\cdot(\widehat{\mathbf{v}\mathbf{v}_h})^{\sim\varpi}\cdot\widehat{\mathbf{v}}_h^{\sim\varpi}]$ | Canonical KE transfer to window $\varpi$ |
| $\Delta Q_P^{\varpi}$ | $-\nabla\cdot\left(\frac{1}{\rho_0}\widehat{\mathbf{v}}^{\sim\varpi}\widehat{P}^{\sim\varpi}\right)$ | Pressure work on window $\varpi$; $P$ is the dynamic pressure related to $\rho$; $\rho_0$ is the reference density of seawater |
| $b^{\varpi}$ | $\frac{g}{\rho_0}\widehat{\rho}^{\sim\varpi}\widehat{w}^{\sim\varpi}$ | Buoyancy conversion on window $\varpi$; $g$ is the gravitational acceleration |
| $A^{\varpi}$ | $\frac{1}{2}c(\widehat{\rho}^{\sim\varpi})^2$, $c = \frac{g^2}{\rho_0^2 N^2}$ | APE on window $\varpi$; $\rho$ is the density anomaly from a reference state $\rho_{\mathrm{r}}(\mathrm{z})$; $N$ is the buoyancy frequency |
| $\Delta Q_A^{\varpi}$ | $-\nabla\cdot\left[\frac{1}{2}c\widehat{\rho}^{\sim\varpi}(\widehat{\mathbf{v}\rho})^{\sim\varpi}\right]$ | APE transport on window $\varpi$ |
| $\Gamma_A^{\varpi}$ | $\frac{c}{2}[(\widehat{\mathbf{v}\rho})^{\sim\varpi}\cdot\nabla\widehat{\rho}^{\sim\varpi} - \widehat{\rho}^{\sim\varpi}\nabla\cdot(\widehat{\mathbf{v}\rho})^{\sim\varpi}]$ | Canonical APE transfer to window $\varpi$ |
| $S_A^{\varpi}$ | $\frac{1}{2}\frac{\partial c}{\partial z}\widehat{\rho}^{\sim\varpi}(\widehat{\rho w})^{\sim\varpi}$ | Apparent source/sink of $A^{\varpi}$ due to the nonlinearity of the reference stratification (usually negligible) |

of multiscale energy and vorticity analysis (MS-EVA; Liang, 2016). The MS-EVA is on the basis of the multiscale window transform (MWT; Liang & Anderson, 2007), which decomposes a function space into several orthogonal subspaces (i.e., scale windows), each with an exclusive time scale range. In a three-window framework (denoted by $\varpi = 0, 1, 2$), a time series $R(t)$ can be reconstructed as:

$$R^{\sim\varpi}(t) = \sum_{n=0}^{2^{j_2}-1}\widehat{R}_n^{\sim\varpi}\phi_n^{j_2}(t), \quad \varpi = 0, 1, 2, \tag{1}$$

where $\widehat{R}_n^{\sim\varpi} = \int_0^1 R^{\sim\varpi}(t)\phi_n^{j_2}(t)dt$ is the MWT coefficient and $\{\phi_n^j(t)\}_n$ is an orthogonal scaling function basis with $j$ ($j_0 < j_1 < j_2$) being the scale level and $n$ ($n = 0, 1, \ldots, 2^{j_2} - 1$) being the time step. In this study, we adopt the MWT to split the original HYCOM data into three scale windows: the nonstationary background flow window (>128 days; $\varpi = 0$), the intraseasonal fluctuation window (8–128 days; $\varpi = 1$), and the high-frequency oscillation window (<8 days; $\varpi = 2$). Note that we use 8–128 days instead of 5–90 days, which is normally defined as the intraseasonal timescale in the SCS (Wang et al., 2020), because the MS-EVA method requires the window bounds to be an exponential function of base 2.

Using the MWT to investigate the dynamics of a hydrostatic and Boussinesq fluid flow, the KE and APE equations on window $\varpi$ can be obtained as:

$$\frac{\partial K^{\varpi}}{\partial t} = \Delta Q_K^{\varpi} + \Gamma_K^{\varpi} + \Delta Q_P^{\varpi} - b^{\varpi} + F_K^{\varpi}, \text{ and} \tag{2}$$

$$\frac{\partial A^{\varpi}}{\partial t} = \Delta Q_A^{\varpi} + \Gamma_A^{\varpi} + b^{\varpi} + S_A^{\varpi} + F_A^{\varpi} \tag{3}$$

where $K^{\varpi}$ and $A^{\varpi}$ denote KE and APE, respectively; $\Delta Q_K^{\varpi}$ ($\Delta Q_A^{\varpi}$) is the KE (APE) transport by advection; $\Delta Q_P^{\varpi}$ is the pressure work closely associated with the distorted isopycnals; $\Gamma_K^{\varpi}$ ($\Gamma_A^{\varpi}$) is the KE (APE) transfer; $b^{\varpi}$ is the buoyancy conversion; $S_A^{\varpi}$ is the apparent source/sink of $A^{\varpi}$ due to the nonlinearity of the reference stratification (usually negligible); the implicit $F$ terms are the residuals including contributions from external forcing, friction, and other unresolved subgrid processes. Note that the definition of $A^{\varpi}$ used here is under the quasigeostrophic (QG) approximation, which assumes the density perturbation is small compared with the horizontally and temporally averaged reference stratification (Lorenz, 1955). The expression and physical meaning of each term in Eqs. (2) and (3) are listed in Table 2, and a detailed derivation can be found in Liang (2016).

Note that the cross-scale transfers $\Gamma^{\varpi}$ in Eqs. (2) and (3) are still in a cumulated form and need to be further decomposed to obtain the interactions between different windows by a technique called "interactions analysis" (Liang & Robinson, 2005). Here we use superscript like 0 → 1 to indicate such interactions. For example, the transfer of KE (APE) from the background flow window ($\varpi = 0$) to the intraseasonal fluctuation window ($\varpi = 1$) is denoted as $\Gamma_K^{0\to1}$ ($\Gamma_A^{0\to1}$). A positive $\Gamma_K^{0\to1}$ ($\Gamma_A^{0\to1}$) means a forward energy cascade and vice versa, which indicates barotropic (baroclinic) instability in the classical geophysical fluid

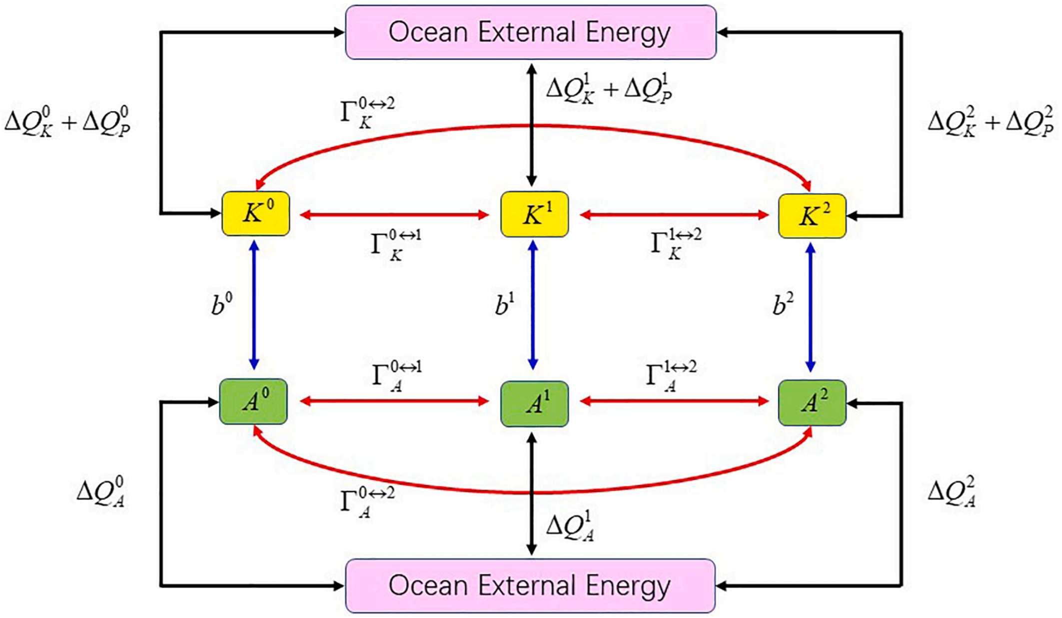

**Fig. 2.** Energy cycle diagram for the local ocean domain in a three-window framework. Red, blue, and black arrows denote the canonical transfers between different scale windows, buoyancy conversions connecting the KE and APE reservoirs, and advective transports, respectively. Note that the forcing/dissipation processes in each window are not shown. Modified from Quan et al. (2021a).

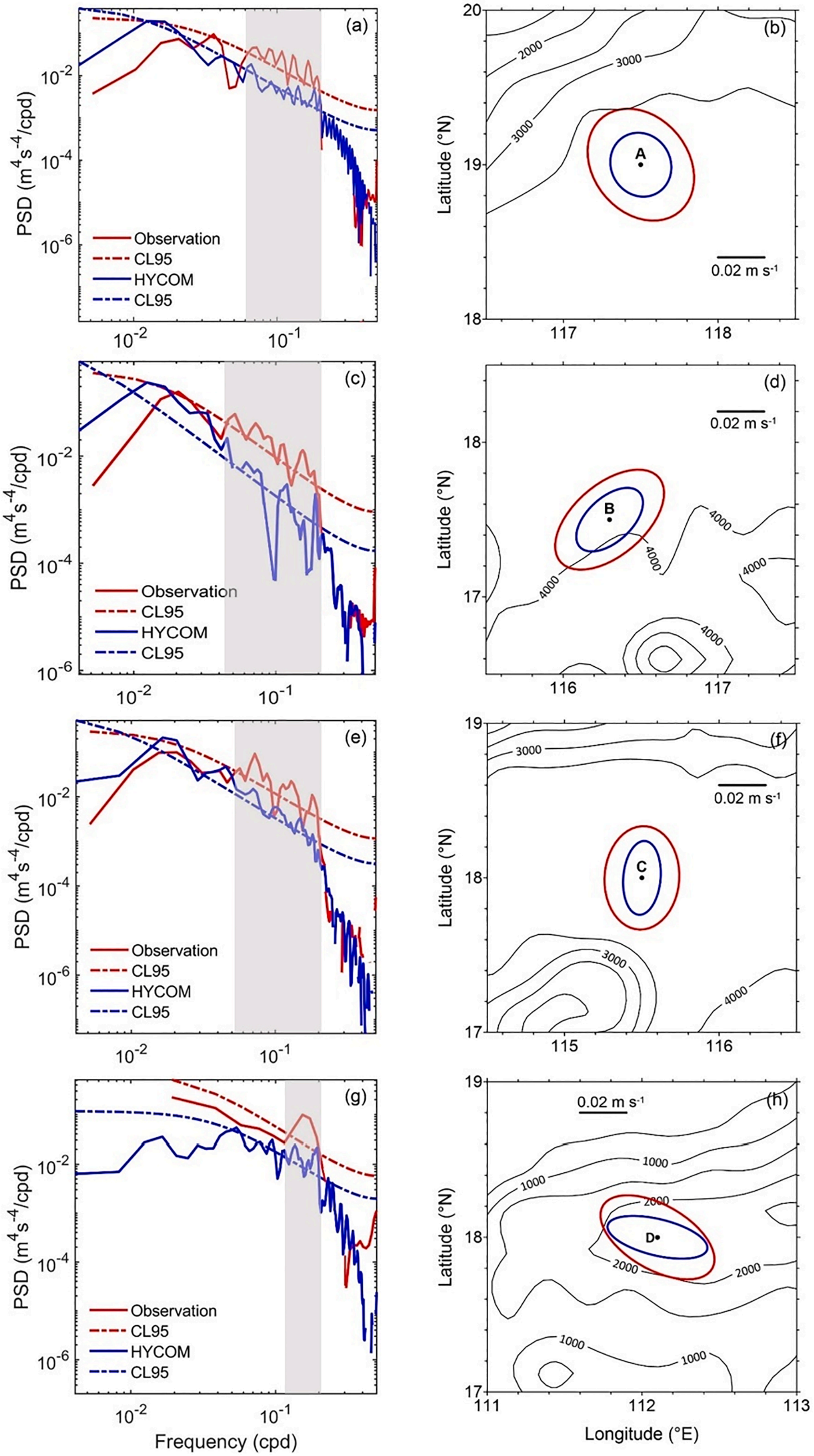

**Fig. 3.** (a) Power spectra of 5–90 days band-passed KE at 100 m above the bottom of site A for observations (red) and HYCOM data (blue). Components significant at the 95% confidence level are shaded. (b) STD ellipses of 5–90 days band-passed velocity at 100 m above the bottom of site A for observations (red) and HYCOM data (blue). Contours denote the isobaths with an interval of 500 m. (c-d), (e-f) and (g-h) are similar to (a-b), but for sites B-D, respectively.

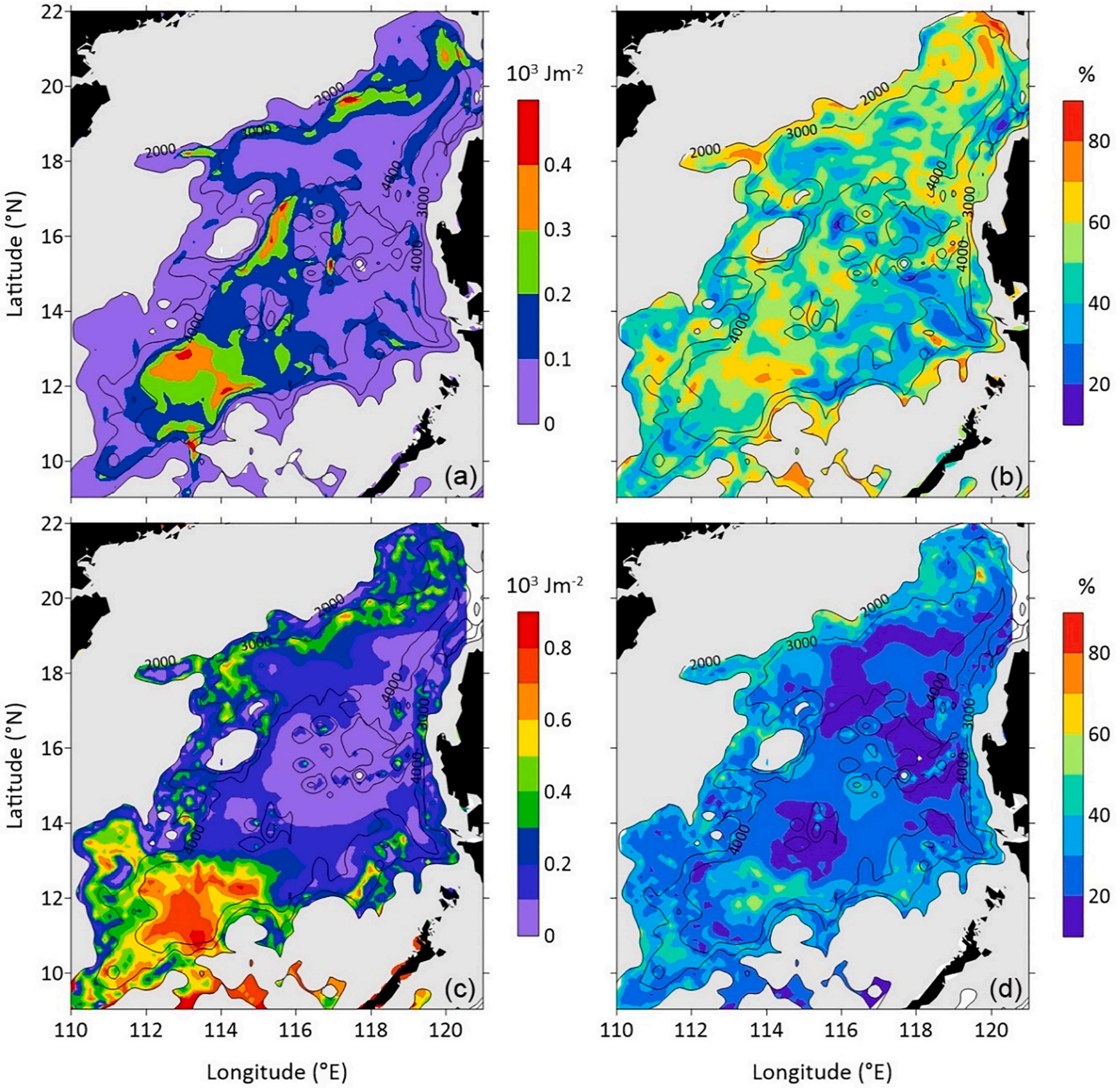

**Fig. 4.** Depth-integrated intraseasonal energy components ($10^3$ J m$^{-2}$) and their contribution to the total STD of (upper) KE and (lower) APE.

dynamics (Liang & Robinson, 2007). Similarly, interactions between window $\varpi = 1$ and $\varpi = 2$ ($\varpi = 0$ and $\varpi = 2$) is written as $\Gamma^{1\rightarrow 2}$ ($\Gamma^{0\rightarrow 2}$). The cross-scale transfers $\Gamma_n^{\varpi}$ possess a vital property:

$$\sum_{\varpi}\sum_{n}\Gamma_n^{\varpi} = 0 \tag{4}$$

where $\sum_{\varpi}$ and $\sum_{n}$ sum over all the scale windows $\varpi$ and sampling time steps $n$, respectively. This is suggestive of a perfect transfer process that merely redistributes energy among scale windows without generating or destroying energy as a whole. This property, though natural, generally does not hold for the previous formalisms. For this reason, the cross-scale interaction $\Gamma^{\varpi}$ has been termed *canonical transfer*. This extraordinary property makes the MS–EVA mathematically and physically complete and become a useful tool to evaluate the multiscale oceanic and atmospheric energy budgets (Liang & Robinson, 2009; Yang & Liang, 2016, 2018; Ma & Liang, 2017; Yang et al., 2017, 2020, 2021).

The energy cycle for the local ocean domain in a three-window framework is schematized in Fig. 2. As mentioned by Liang (2016), the canonical transfers bridge different windows and represent the cross-scale processes, such as instabilities, while the buoyancy conversions and transports function only within respective individual windows. The former links the KE and APE, and the latter allows different spatial locations to communicate. In this study, we apply the MS-EVA to examine the relative importance of these processes in the energetics of the abyssal SCS. In the following, we will focus on the results from the window $\varpi = 1$ (variables with the superscript "1″). Note that the energy components and energetics are multiplied by a reference density $\rho_0 = 1025$ kg m$^{-3}$ and shown in units of J m$^{-3}$ and W m$^{-3}$, respectively.

## 3. Spatiotemporal characteristics

In this section, we investigate the spatiotemporal characteristics of intraseasonal fluctuations in the abyssal SCS to determine their energy reservoir, dynamics, and instability.

### 3.1. Energy reservoir

Consistent with the previous studies (Shu et al., 2016; Zhou et al., 2017; Wang et al., 2019), the observations also indicate persistent and energetic intraseasonal fluctuations in the abyssal SCS (Fig. 3). Spectral analysis of 5–90 days band-passed deep KE demonstrates that components significant at the 95% confidence level generally concentrate in a period band of 5–60 days that varies with space (shaded red solid lines in the left panel of Fig. 3). The corresponding standard deviation (STD) ellipses of the deep velocities show a major principal axis comparable to

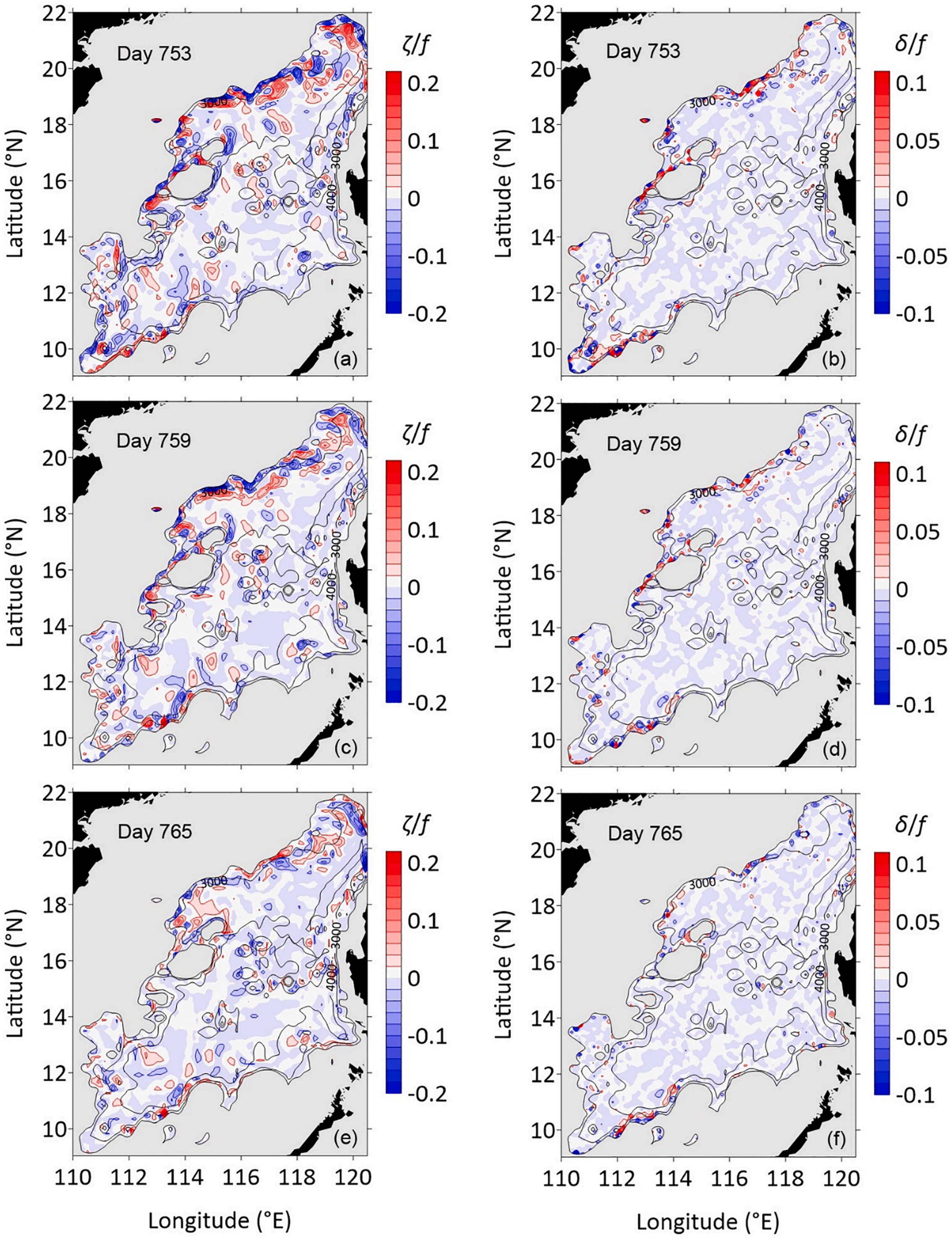

**Fig. 5.** Snapshots of relative vorticity $\zeta^1$ and divergence $\delta^1$ (normalized by $f$) at 2500 m from days 753 to 765 with a 6-day interval.

the mean flow (not shown) and parallel to the local isobath or roughly north–south oriented (red ellipses in the right panel of Fig. 3), indicating that the deep flow oscillates along topography or meridionally.

As shown in our recent studies (Quan et al., 2021a, b), the HYCOM reanalysis largely reproduces the features observed in the intraseasonal variability of deep flow in the SCS. The spectra of subinertial motions in the HYCOM are close to the observations despite a weaker intensity (shaded blue solid lines in the left panel of Fig. 3). This is also reflected by the analogous but smaller STD ellipses of the modeled deep velocities (blue ellipses in the right panel of Fig. 3). Although the model quantitatively underestimates the intraseasonal fluctuations in the abyssal SCS, it is believed to qualitatively reveal the deep flow variability and the underlying dynamics. The latter, in turn, could help determine the key process that is important for improving the model performance in the abyssal marginal seas (e.g., Morey et al., 2020).

Based on the analysis above, we then use the HYCOM data to examine the basin-wide energy reservoir in the deep SCS. Fig. 4 exhibits the intraseasonal energy components (i.e., $K^1$ and $A^1$) integrated from the bottom to 2000 m and their contributions to the variability of total energy in the deep SCS. In the horizontal plane, both the energy components are distributed inhomogeneously, with $A^1$ generally larger than $K^1$ (Fig. 4a and 4c). Similar to that observed in the deep Gulf of Mexico (Oey & Lee, 2002), the high energy density resides in a topography–trapped strip along the continental slopes of the abyssal SCS, with several hot spots northwest of the Luzon Strait, northern slopes, DWBC region, and southwestern cyclonic gyre region. In contrast, both $K^1$ and $A^1$ are weak in the interior basin.

To highlight the importance of the intraseasonal fluctuations in accounting for the deep-current variability, we calculate the ratio of the STD of $K^1$ ($A^1$) to the STD of the total KE (APE). Fig. 4b demonstrates that the ratios for KE are more than 40% over the steep topography of the deep SCS, with the maximum reaching 70% over the hot spots mentioned above. With a pattern similar to that of the KE, the ratios for APE are smaller (Fig. 4d). The model results indicate that intraseasonal fluctuations contribute greatly to the deep-current variability in the SCS, which is consistent with the observations (Shu et al., 2016; Zhou et al., 2017; Wang et al., 2019; Zhou et al., 2020; Zheng et al., 2021).

### *3.2. Dynamics*

Geographical inhomogeneity of energy is suggestive of the intrinsic dynamics of intraseasonal fluctuations in the abyssal SCS. To visualize these subinertial motions in the deep SCS, Fig. 5 exhibits the snapshots of the relative vorticity $\zeta^1$ and divergence $\delta^1$ (normalized by the Coriolis parameter $f$) at 2500 m from day 753 to day 765 with a 6-day interval (note that in this paper we use day numbers for convenience). The vorticity pattern is characterized by alternating cyclonic–anticyclonic meanders over the sloping topography (e.g., in the northern slope region) and in the interior basin (e.g., along 18°N). The absolute values of the normalized relative vorticity (i.e., the Rossby number) are generally less than 0.2, suggesting the validity of QG dynamics. Correspondingly, the horizontal motions are weakly divergent except for several areas, such as the slopes south of the Dongsha Islands, slopes northwest of the Zhongsha Islands, and western slopes in the south, where the topography is exceptionally steep. According to the incompressibility, the vertical motions tend to be active in these regions, which can reach $O(10^{-3})$ m s$^{-1}$ (not shown) and contribute greatly to the cross-slope exchange (Wang et al., 2020).

According to Rhines (1970), the QG dispersion relation in the case with constant stratification can be expressed by two coupled equations:

$$\lambda_\nu^2 = \left(k^2+l^2+\frac{\beta k}{\omega}\right)\left(\frac{N}{f}\right)^2, \text{ and} \tag{5}$$

$$\omega = (\mathbf{L}\times\nabla h)\frac{N^2}{\lambda_\nu f}\coth(\lambda_\nu h) \tag{6}$$

where $\lambda_\nu^{-1}$ is the vertical trapping scale, $\mathbf{L}=(k,l)$ is the horizontal wavenumber vector ($L^2 = k^2 + l^2$), $h$ is the water depth, $\nabla h$ is the topographic gradient, and $\omega$ is the frequency. Eqs. (5) and (6) represent the hybrid topographic-planetary Rossby waves. The waves are dominated by TRWs when the topographic beta $\beta_{top} = f|\nabla h|/h$ overwhelms the planetary beta $\beta = \partial f/\partial y$, and the dispersion relation can then be rewritten as.

$$\omega = (\mathbf{L}\times\nabla h)\frac{N}{L}\coth(\lambda_\nu h) \tag{7}$$

Otherwise, the waves will turn into pure planetary Rossby waves (PRWs) following the dispersion relation as.

$$\omega = -\frac{\beta k}{k^2+l^2+\frac{m^2}{L_D^2}}, \quad m=0,1,2,\ldots \tag{8}$$

where $L_D = Nh/f$ is the internal Rossby deformation radius, and $m$ is the mode number ($m = 0$ for the barotropic mode and others for the baroclinic modes).

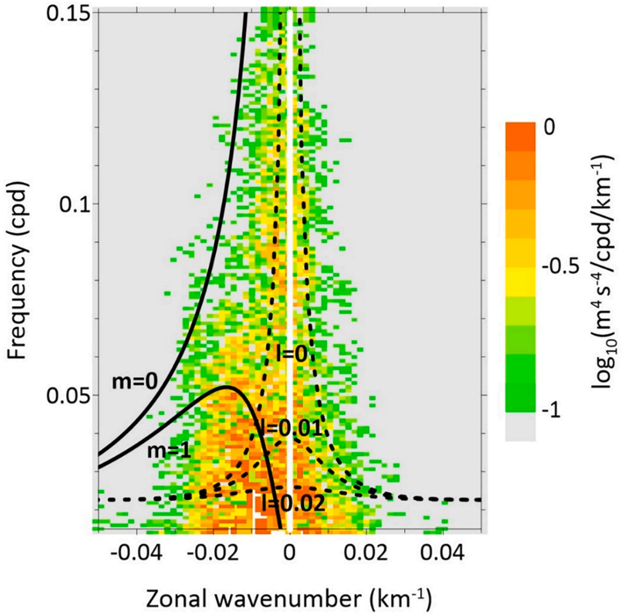

**Fig. 6.** Zonal wavenumber–frequency spectrum of $K^1$ at 2500 m averaged over five longitude-time sections from 12°N to 20°N with an interval of 2°. Note that the values smaller than −1 are masked. Black solid (dashed) lines are the theoretical dispersion curves of the PRWs (TRWs) based on typical parameters in the deep SCS.

In the deep SCS, the observed buoyancy frequency $N$ is largely constant or a weak function of depth (Wang et al., 2019), which makes the abovementioned theory generally valid. To determine the dynamics of these subinertial motions, we examine the dispersion relations in Eqs. (7) and (8) by estimating the zonal wavenumber–frequency spectrum of $K^1$ at 2500 m. In light of Farrar (2008), the computation is conducted by a 2D fast Fourier transform at five zonal sections (110°E-120°E; grids with a water depth shallower than 2500 m are excluded) from 12°N to 20°N with an interval of 2°. To highlight the variability of $K^1$, the zonal-temporal mean is removed from each longitude-time section. Then we taper the edges of each section to zero with a half-Hanning window over 90 days and 20 km to minimize the spectral leakage. Since the dispersion characteristics are largely dependent on the latitude, topography and stratification, the spectra are averaged over the five sections to improve the statistical significance and the results are shown in Fig. 6. The power spectral density (PSD) is elevated generally along the theoretical dispersion curves of PRWs (mostly in the first baroclinic mode $m = 1$) and TRWs for the typical parameters in the deep SCS ($N = 1.0\times10^{-3}$ s$^{-1}$, $h = 3000$ m,$|\nabla h| = 0.02$, $f = 4\times10^{-5}$ s$^{-1}$, and $\beta = 2\times10^{-11}$ m$^{-1}$s$^{-1}$). The space-dependent periods range from 5 to 90 days, and the low-frequency components appear to dominate the spectra. According to the instability theory (McWilliams, 2011), the wavelength of the most unstable waves is scaled by the internal Rossby deformation radius $L_D$. In the deep SCS, the typical $L_D$ is approximately 70 km. Consequently, the PSD tends to peak at wavelengths of approximately 100 km or longer. The spectral analysis indicates that the intraseasonal fluctuations in the abyssal SCS are dominated by hybrid topographic–planetary Rossby waves. These subinertial waves have been suggested to be critical to the generation and evolution of the abyssal circulation, as well as the dynamic coupling between the upper and middle layers of the SCS (Quan & Xue, 2018, 2019).

### *3.3. Instability*

Because the QG motions contribute substantially to the energy dissipation in both open ocean and marginal seas (von Storch et al.,

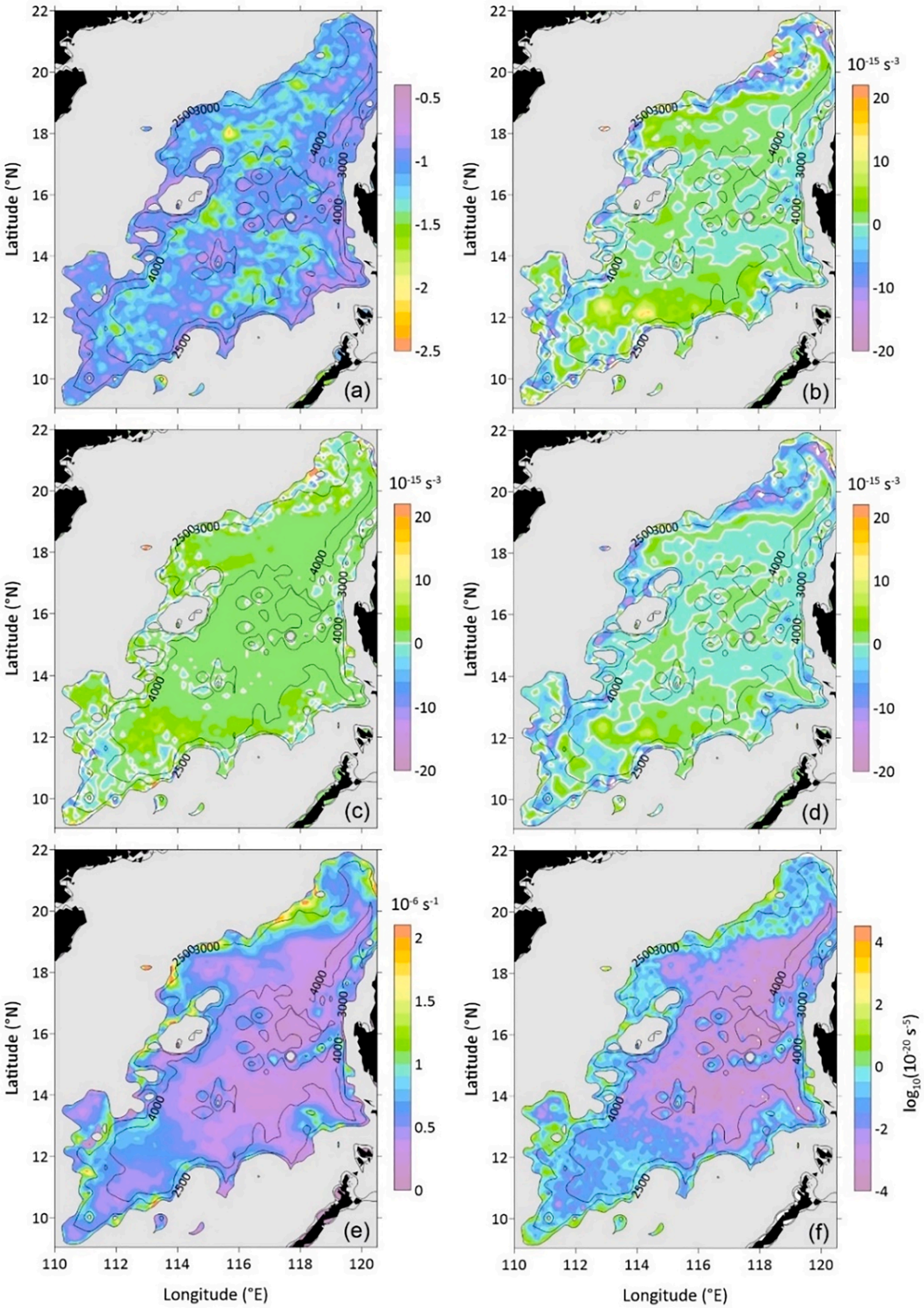

**Fig. 7.** Horizontal distributions of (a) skewness of relative vorticity, (b) $Q_{Ertel}$ ($10^{-15}$ s$^{-3}$), (c) $Q_{vert}$ ($10^{-15}$ s$^{-3}$), (d) $Q_{bc}$ ($10^{-15}$ s$^{-3}$), (e) strain rate ($10^{-6}$ s$^{-1}$), and (f) frontogenesis function ($10^{-20}$ s$^{-5}$) at 2500 m. Note that the zero contour is highlighted in (b-d) to distinguish between positive and negative values.

2012; Maslo et al., 2020), another perspective on characterizing the intraseasonal fluctuations in the deep SCS is to evaluate the instability of the flow field that could lead to energy dissipation.

We first calculate the skewness of the relative vorticity $\zeta^1$ at each grid, which measures the asymmetry of the probability density function (PDF) of $\zeta^1$. A large $\zeta^1$ skewness implies an extremely strong $\zeta^1$ that occurs occasionally, manifested as a long tail in the distribution of the PDF. This kind of skewness is usually ascribed to instability. For example, the occurrence of centrifugal instability (defined later) requires a negative absolute vorticity (i.e., $\zeta^1/f < -1$ when $f > 0$), which efficiently restricts the continuous growth of extreme negative $\zeta^1$ but would not affect the positive $\zeta^1$. As a result, a positive $\zeta^1$ skewness is commonly gained when the centrifugal instability occurs (Klein et al., 2008; Mensa et al., 2013; Zhong & Bracco, 2013). Similar to other results away from the surface, for example, in the California Undercurrent (Molemaker et al., 2015), Fig. 7a reveals that the skewness of $\zeta^1$ at 2500 m is always negative, indicating that the sporadic intense negative $\zeta^1$ is preferred in the deep SCS. The elevated values over the northern slopes and in the DWBC region probably arise from topographic drag, which can produce strong negative vorticity to its anticyclonic side due to the flow–topography interactions (Molemaker et al., 2015; Gula et al., 2016). This may explain the generation of the strong negative $\zeta^1$, but how the vorticity can be maintained requires further investigation.

To answer this question, we examine the instability type of intraseasonal fluctuations in the deep SCS. According to the instability theory (Pedlosky, 1987; McWilliams, 2011), the criterion of instability is related to the spatial sign reversal of the Ertel PV, defined as.

$$Q_{Ertel} = \underbrace{\left(-\frac{\partial v}{\partial z}+\frac{\partial w}{\partial y}\right)\frac{\partial B}{\partial x}+\left(\frac{\partial u}{\partial z}-\frac{\partial w}{\partial x}\right)\frac{\partial B}{\partial y}}_{Q_{bc}}+\underbrace{(f+\zeta)N^2}_{Q_{vert}} \tag{9}$$

where $B = -g\rho/\rho_0$ is the buoyancy. A variety of instabilities arise when $f\cdot Q_{Ertel} < 0$, for example, $Q_{Ertel} < 0$ in the Northern Hemisphere (Hoskins 1974). These instabilities take different names depending on whether the vertical vorticity, stratification, or baroclinicity of the fluid is responsible for the low $Q_{Ertel}$. Here we decompose $Q_{Ertel}$ into two terms, one associated with the buoyancy gradient (i.e., $Q_{bc}$), and the other attributable to the absolute vorticity and stratification (i.e., $Q_{vert}$). When $Q_{bc} < 0$ and $|Q_{bc}| > Q_{vert}$ with $Q_{vert} > 0$, symmetric instability occurs; the occurrence of centrifugal instability is related to the barotropic shear and requires a negative absolute vorticity (i.e., $f + \zeta < 0$) with $N^2 > 0$; the instability is termed gravitational when $N^2 < 0$ (Thomas et al., 2013). To obtain a statistical insight into the state of flow field, Fig. 7b shows the horizontal map of $Q_{Ertel}$ at 2500 m averaged within the data period. Results indicate that $Q_{Ertel}$ tends to be negative over the sloping topography, suggesting the instability of flow in these regions. Because the square of buoyance frequency $N^2$ is positive in the abyssal SCS (not shown) and the absolute value of the normalized relative vorticity (i.e., $\zeta^1/f$) is mostly smaller than 1 (left panel in Fig. 5), the component associated with the absolute vorticity and stratification (i.e., $Q_{vert}$) is largely positive (Fig. 7c), indicating that the gravitational and centrifugal instability rarely occurs in the deep SCS. This may account for the negative $\zeta^1$ skewness in Fig. 7a because of the absence of centrifugal instability to suppress the growth of exceptional negative vorticity (Lin et al., 2020; Zhang et al., 2020). In contrast, the component related to the baroclinicity of flow (i.e., $Q_{bc}$) dominates the overall pattern of $Q_{Ertel}$, particularly in the slope regions (Fig. 7d). This suggests that the intraseasonal fluctuations in the deep SCS appear to be of symmetric instability, primarily owing to the vertical shear of horizontal velocity and horizontal buoyancy gradient. This result is consistent with the finding that the TRWs in these regions can induce a columnar (i.e., in-phase) current with the speed increasing toward the bottom (Quan et al., 2021a). One may question whether symmetric instability at such depths seems to be at odds with the classical paradigm. According to the geostrophic turbulence theory, the loss of balance (e.g., frontogenesis) to dissipate the geostrophic EKE is possible only at the surface rather than in the deep layer because the surface modes at small scales do not interact efficiently with the interior modes and do not barotropize (Capet et al., 2008; Ferrari & Wunsch, 2009; Molemaker et al., 2010). However, a recent study by Siegelman (2020) suggested that the ocean interior down to 900 m is strongly ageostrophic, with a pronounced cyclone–anticyclone asymmetry and a dominance of frontogenesis over frontolysis. Our results coincide with this finding and imply the possible energy dissipation for intraseasonal motions through symmetric instability in the abyssal SCS.

To further reveal the potential cascade from the intraseasonal fluctuations to smaller scales in the deep SCS, we calculate the strain rate (SR) defined as.

$$SR = \sqrt{\left(\frac{\partial u}{\partial x}-\frac{\partial v}{\partial y}\right)^2+\left(\frac{\partial u}{\partial y}+\frac{\partial v}{\partial x}\right)^2} \tag{10}$$

which is an index for the deformation of mesoscale currents that can intensify the fronts through frontogenesis (McWilliams, 2016). Fig. 7c displays the distribution of the long-term mean SR at 2500 m. The results are one order of magnitude smaller than those in the surface layer (Lin et al., 2020; Zhang et al., 2020), and the values are elevated over the steep topography. Because the strong $|\nabla B|$ tends to reside in the strain-dominated region (Thomas et al., 2013; Siegelman, 2020), Fig. 7d and 7e share a similar pattern. This suggests that the weak lateral shear in the deep SCS can hardly lead to centrifugal instability, but indirectly contributes to the symmetric instability by enhancing the horizontal buoyancy gradient. The rate of this process is quantified by the frontogenesis function as follows:

$$F_{front} = 2\mathbf{Q}\cdot\nabla_h B = \frac{d}{dt}|\nabla_h B|^2 \tag{11}$$

where

$$\mathbf{Q} = \left(-\frac{\partial \mathbf{v}}{\partial x}\cdot\nabla_h B - \frac{\partial \mathbf{v}}{\partial y}\cdot\nabla_h B\right) \tag{12}$$

Fig. 7f demonstrates that $F_{front}$ is elevated in the regions where both SR and symmetric instability are pronounced, of which the magnitude is comparable to that in the deep Antarctic Circumpolar Current (Siegelman, 2020). The symmetric instability is thought to extract energy from the geostrophic fronts and transfer to smaller scales, contributing to the local mixing (Taylor & Ferrari, 2009; Buckingham et al., 2019). Although the effect that frontogenesis enhances the horizontal buoyancy gradient to drive the symmetric instability is weak, the process provides a potential route to initiate a forward cascade of the intraseasonal energy down to dissipation in the abyssal SCS.

Taken together, the intraseasonal fluctuations in the abyssal SCS are supposed to be symmetrically unstable. However, the submesoscale processes cannot be resolved by the present model. Consequently, the energy transfer between windows $\varpi = 1$ and $\varpi = 2$ (i.e., $\Gamma^{1\to2}$) is not significant as expected. As a residual in the diagnosis, the viscous parameterization blends the unresolved subgrid processes and becomes a primary sink in the energy budget, which can be verified by the elevated negative $F_K^1$ in the regions where the SR is prominent (see the details in section 4). Limited by the model resolution, it should be noted that the results can only be taken as a state indicator of the modeled flow field, rather than full information for symmetric instability in the realistic ocean (e.g., Dong et al., 2021).

## 4. Energetics

Now that we have revealed the spatiotemporal characteristics of the intraseasonal fluctuations in the abyssal SCS, we investigate the relevant energetics in this section. To highlight the underlying dynamics, we categorize the terms in Eqs. (2) and (3) to the nonlocal processes ($\Delta Q_P^1$,$\Delta Q_K^1$, and $\Delta Q_A^1$), local processes ($\Gamma_K^1$,$\Gamma_A^1$, and $b^1$), and implicit processes ($F_K^1$ and $F_A^1$). All the results are integrated from the bottom to 2000 m and averaged over the data period.

### 4.1. Nonlocal processes

The nonlocal processes are closely associated with the physical fluxes

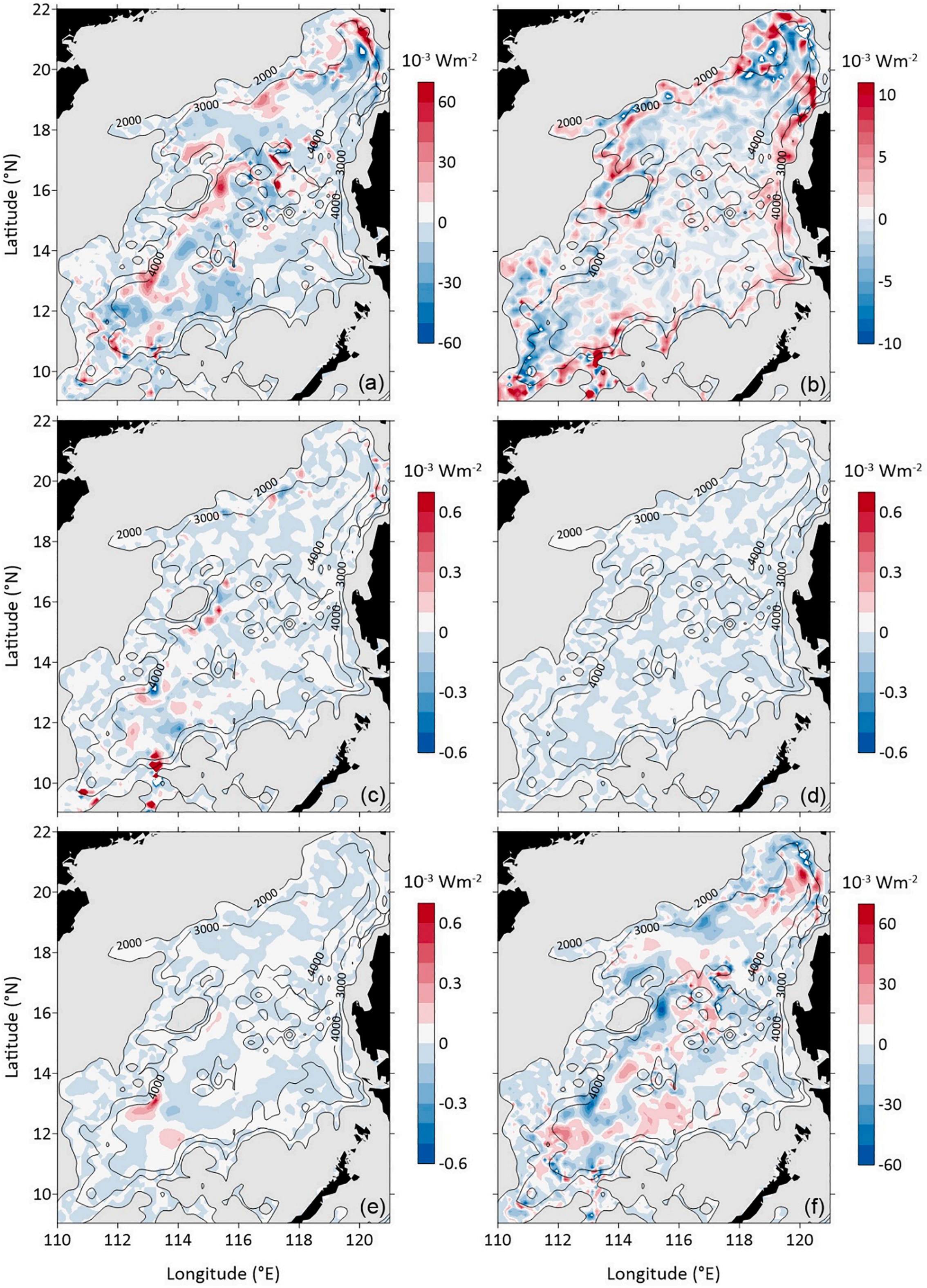

**Fig. 8.** Depth-integrated $K^1$ energetics ($10^{-3}$ W m$^{-2}$) from the bottom to 2000 m for (a)$\Delta_h Q_P^1$, (b)$\Delta_z Q_P^1$, (c)$\Delta_h Q_K^1$, (d)$\Delta_z Q_K^1$, (e)$\Gamma_K^{0\to1}$, and (f)$F_K^1$.

in the flow field, including the pressure work ($\Delta Q_P^1$) and energy transport ($\Delta Q_K^1$ and $\Delta Q_A^1$). Following previous studies, we also divide the pressure work into horizontal and vertical components, i.e., $\Delta_h Q_P^1$ and $\Delta_z Q_P^1$, to examine their contributions to the intraseasonal energetics of the deep SCS. Collocated with the distribution of high $K^1$, the positive $\Delta_h Q_P^1$ is concentrated northwest of the Luzon Strait, southeast of the Dongsha Islands, the DWBC region, and the periphery of the southwestern cyclonic gyre, whereas the negative values predominantly exist in the interior basin where the topography is smooth (Fig. 8a). This indicates that the horizontal pressure work tends to radiate $K^1$ onshore and shape the high-energy zone along the steep slopes, which is

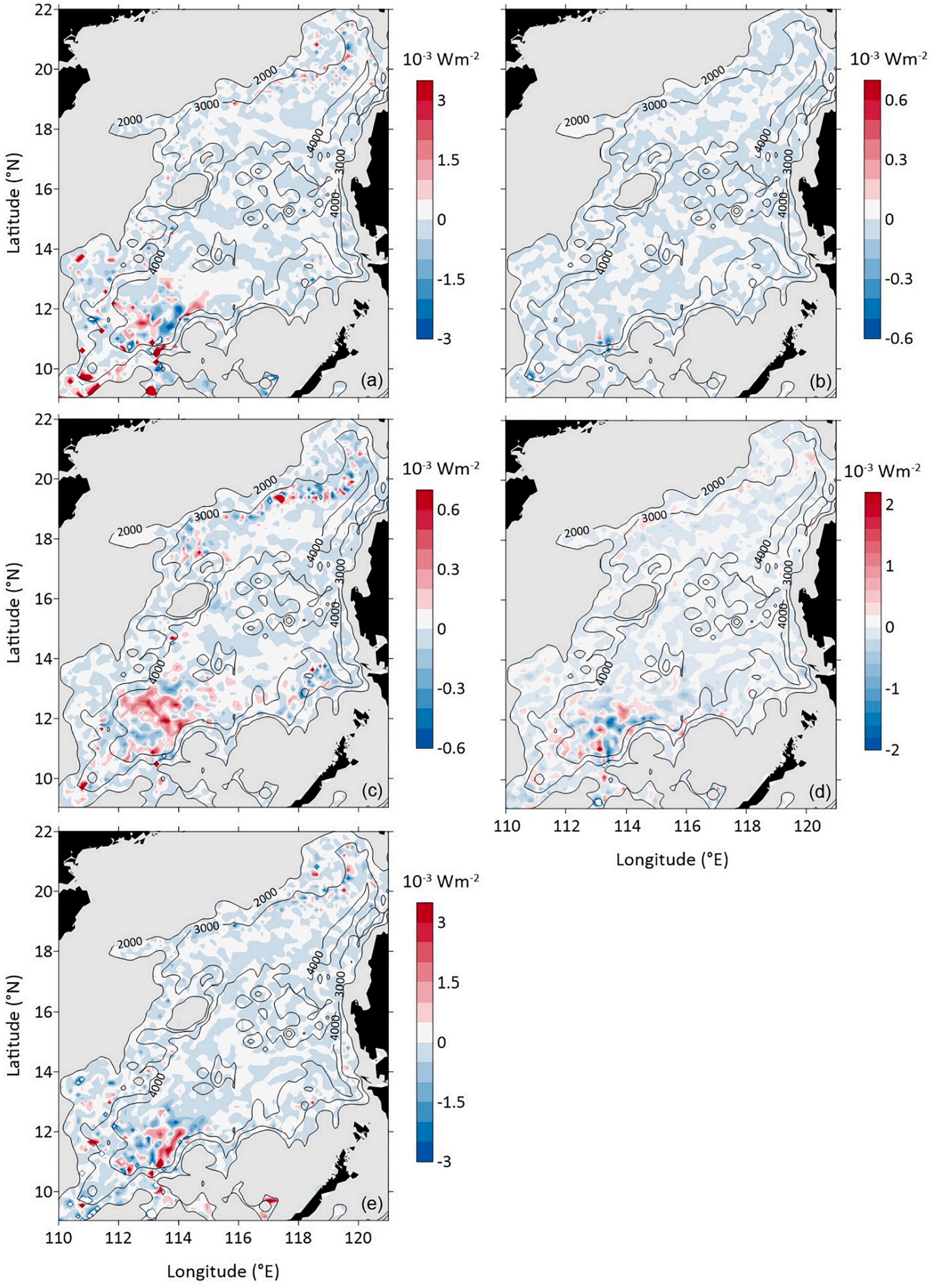

**Fig. 9.** Depth-integrated $A^1$ energetics ($10^{-3}$ W m$^{-2}$) from the bottom to 2000 m for (a)$\Delta_h Q_A^1$, (b)$\Delta_z Q_A^1$, (c)$\Gamma_A^{0\to 1}$, (d)$b^1$, and (e)$F_A^1$.

consistent with the results in the Gulf of Mexico (Yang et al., 2020). Smaller than the horizontal counterpart, the positive vertical pressure work $\Delta_z Q_P^1$ is distributed widely over the entire deep SCS and peaks over the steep topography (Fig. 8b). Because of the opposite signs between the horizontal and vertical components of pressure work, the positive $\Delta_z Q_P^1$ is weak in the DWBC region but intensive over the northern and southern slopes. These results suggest that pressure work is critical for regulating the intraseasonal KE in the deep SCS, particularly in the slope regions. This is consistent with the recent study by Quan et al. (2021b) that TRWs in the northern SCS are primarily energized by the Kuroshio intrusion and the related eddies, which can significantly deform the isopycnal to radiate energy downward through pressure work. Since the

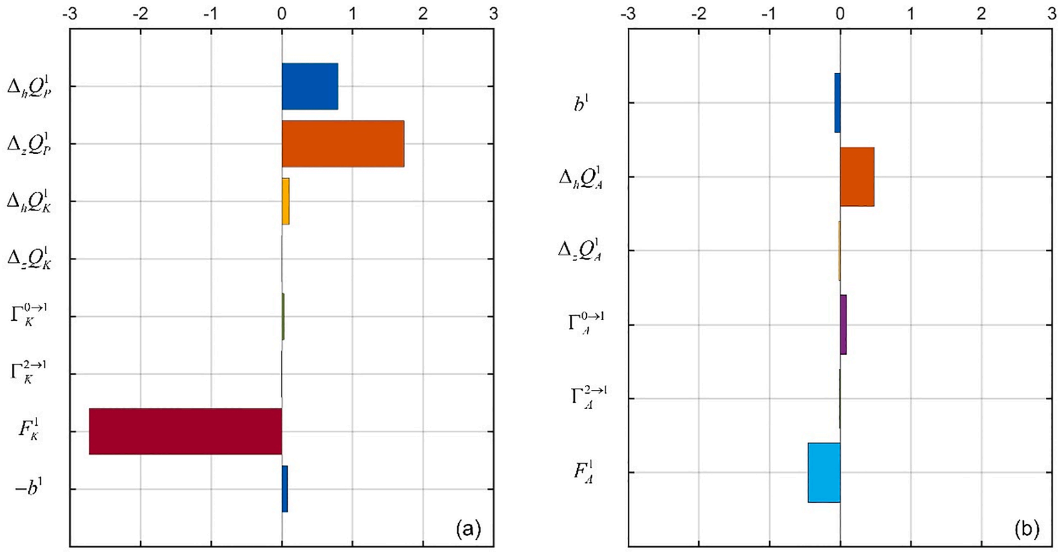

**Fig. 10.** Energy budget (GW; 1 GW = $10^9$ W) for (a) $K^1$ and (b) $A^1$. Results are integrated over the abyssal SCS from the bottom to 2000 m and averaged in the data period.

present work focuses on the evaluation of energy balance in the abyssal SCS, the details for how the pressure work functions can be found in the appendix and the relevant process analysis can be referred to Quan et al. (2021a).

The energy transports ($\Delta Q_K^1$ and $\Delta Q_A^1$) are the other nonlocal processes that redistribute KE and APE in the abyssal SCS. Similarly, we also divide these advection terms into horizontal and vertical components. By comparing Fig. 8c and 8e (Fig. 9a and 9c), it is found that both $\Delta_h Q_K^1$ and $\Delta_h Q_A^1$ are pronounced in the regions where the cross-scale energy transfers are active. In these areas, the advective transport and the cross-scale transfer are usually opposite in sign, suggesting that the energy gained from a forward cascade tends to be advected downstream to support an inverse cascade. For example, in the southwest where the DWBC separates from the topography, both KE and APE extracted from the background flow are transported to sustain the subbasin gyres on both sides of the DWBC. This is similar to the scenario in the Gulf of Mexico, where the EKE derived from the upstream of the Loop Current is carried to the downstream region to feed back to the background flow (Yang et al., 2020). Both the vertical components $\Delta_z Q_K^1$ and $\Delta_z Q_A^1$ are much weaker than their horizontal counterparts (Fig. 8d and 9b), suggesting that the vertical energy transport can be ignored here.

These results suggest that pressure work plays a key role in redistributing the intraseasonal energy in the abyssal SCS, both horizontally and vertically, while the effect of energy transport is secondary. This is consistent with the previous study in which the pressure work contributes greatly to the redistribution of the eddy energy in open oceans (Zhai & Marshall, 2013). Considering the opposite signs between layers, the pressure work, which acts as a sink of EKE in the upper ocean (Chen et al., 2014), now becomes a primary source of intraseasonal energy in the abyssal SCS.

### 4.2. *Local processes*

The local processes include cross-scale energy transfers ($\Gamma_K^1$ and $\Gamma_A^1$) and the conversion between KE and APE ($b^1$). Although the energy from cross-scale transfers is considerable during some specific events (Quan et al., 2021a), its long-term integration is relatively weak in the deep SCS. The positive barotropic transfer $\Gamma_K^{0\to1}$ occurs mainly in the DWBC region and peaks in the regions where the DWBC separates from the topography near 113°E, 13°N and joins again with the northeastward branch of the southwestern cyclonic gyre at 114°E, 12°N (Fig. 8e). This suggests that the large-scale deep circulation is barotropically unstable in these regions and releases KE to intraseasonal motions (i.e., $K^0 \to K^1$). Conversely, there exist weak negative pools of $\Gamma_K^{0\to1}$ on both sides of the DWBC in this region, implying an inverse energy cascade from the intraseasonal motions to the background flow (i.e., $K^1 \to K^0$).

In comparison with the weak barotropic transfer, the baroclinic transfer seems to be more active in the abyssal SCS (Fig. 9c). Because the steep topography has been suggested to effectively suppress the baroclinic instability (LaCasce, 1998; LaCasce et al., 2019), the positive $\Gamma_A^{0\to1}$ occurs primarily in two regions, the lower portion of the northern slopes and the separation zone of the DWBC in the southwest, suggesting that the APE in these regions is transferred from the background circulation to the intraseasonal fluctuations (i.e., $A^0 \to A^1$). Following by a negative $b^1$ in these regions (Fig. 9d), the gained APE is then converted to KE to fulfill the baroclinic energy pathway (i.e., $A^0 \to A^1 \to K^1$). Similar to the inverse cascade for KE, a negative $\Gamma_A^{0\to1}$ also occurs in the immediate vicinity. For example, there are negative pools of $\Gamma_A^{0\to1}$ on both sides of the DWBC when the flow separates from the topography, suggesting that the intraseasonal APE is inversely cascaded to the subbasin gyres. Similar upscale energy cascades have also been found in the world oceans where the jet separates from the topography, such as the Gulf Stream Extension, Kuroshio Extension, and California Undercurrent (Kang & Curchitser, 2015; Yang & Liang, 2016; Molemaker et al., 2015).

Although the intraseasonal motions in the abyssal SCS are suggested to be of symmetric instability, the cross-scale transfers between the intraseasonal window and the high-frequency window (i.e., $\Gamma_K^{1\to2}$ and $\Gamma_A^{1\to2}$) are very weak (not shown) because of the limited model resolution. The subgrid processes are likely to blend within the parameterized viscosity. Such problems have been extensively discussed in previous studies, but for now, there is no perfect solution even for submesoscale-resolved models (e.g., Molemaker et al., 2015; Gula et al., 2016; Zhang et al., 2020; Yang et al., 2021). Hence, the weak interactions between windows $\varpi = 1$ and $\varpi = 2$ should be carefully evaluated in the present study.

### 4.3. *Implicit processes*

The implicit terms $F_K^1$ and $F_A^1$ include the contributions from external forcing, friction, and other unresolved subgrid processes, which are involved in the parameterized viscosity (Fig. 8f and 9e). In a dynamic sense, the depth-integrated $F_K^1$ can be regarded as the net work of viscous

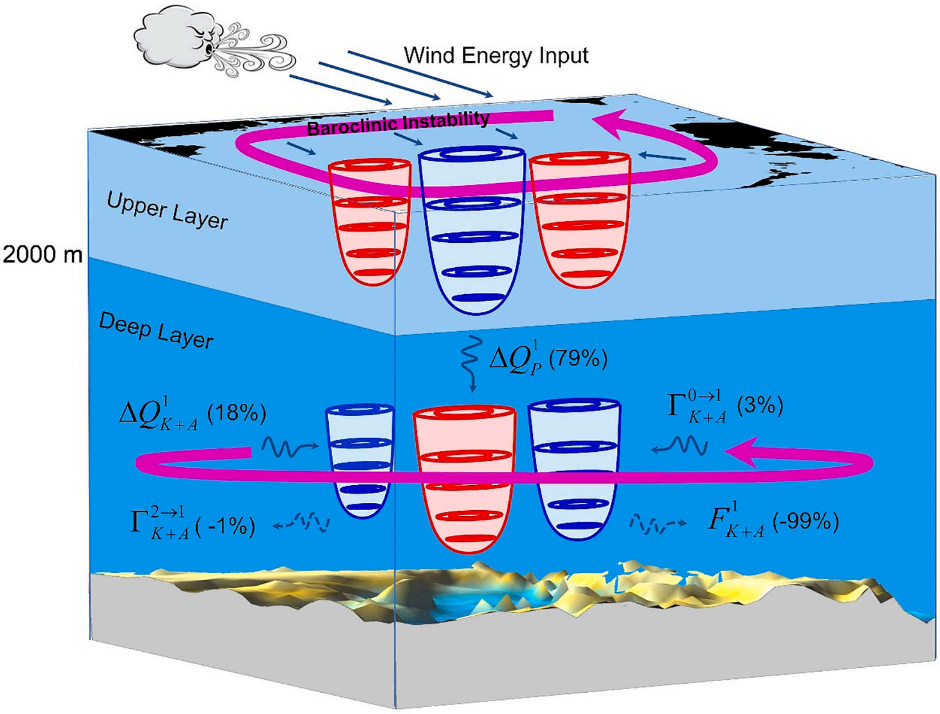

**Fig. 11.** Schematic diagram of the intraseasonal energetics of the abyssal SCS. The water column is roughly separated by 2000 m. The upper layer is visually squeezed to highlight the sketch of energy budget in the deep layer. Contributions from each mechanical energy source (positive) and sink (negative) are illustrated. The magenta streamlines denote the vertically-integrated cyclonic circulations in the upper and deep layers. The eddy-like graphics represent the general intraseasonal processes with an alternating positive (red)-negative (blue) vorticity pattern that are controlled by PV conservation (cf., Oey, 2008).

stresses executing on the upper and lower surfaces, which tends to offset the pressure work in the balance of $K^1$. The negative $F_K^1$ is generally elevated in the slope region, whereas it is positive in areas with a smooth topography. This implies that $F_K^1$ is dominated by dissipation (forcing) process and acts as a sink (source) of KE over the sloping topography (in the interior basin). The maximum $K^1$ dissipation rate can reach $6 \times 10^{-8}$ $m^2\ s^{-3}$ ($W\ kg^{-1}$) over the steep slope, which is comparable to that induced by tides in the deep SCS (X. Wang et al., 2016). By comparing Fig. 7b and 8f, the occurrence of instability brings with it the potential for enhanced diapycnal mixing and dissipation, consistent with previous studies (Molemaker et al., 2010; Dewar et al., 2015; Gula et al., 2016; Zhang et al., 2020). Unfortunately, the forward cascade down to dissipation cannot be distinguished from the viscous parameterization in the present model.

Much weaker than $F_K^1$, the depth-integrated $F_A^1$ can be regarded as the diapycnal flux of APE owing to the mixing-induced entrainment/detrainment. The elevated $F_A^1$ over the northern slopes and in the southwestern cyclonic gyre region also corresponds well to the generation of symmetric instability, as shown in Fig. 7d. Similar to the Gulf of Mexico (Maslo et al., 2020), $F_A^1$ is mostly balanced by $\Delta Q_A^1$ in the abyssal SCS.

### 4.4. Energy budget

The results above exhibit substantial geographical inhomogeneity in the intraseasonal energetics of the abyssal SCS. To determine the energy budget in the entire domain, we integrate the results in Figs. 8 and 9 over the deep SCS (Fig. 10). The results indicate that the pressure work serves as the major source of $K^1$, with its vertical component $\Delta_z Q_P^1$ approximately twice that of its horizontal counterpart $\Delta_h Q_P^1$. The KE advection $\Delta_h Q_K^1$ and the buoyancy conversion $b^1$ also supply KE to the abyssal SCS, but their contributions are much less than the pressure work. In a similar order of magnitude with the estimations in the Gulf of Mexico (e.g., Yang et al., 2020; Maslo et al., 2020), the net barotropic transfers ($\Gamma_K^{0\to1}$ and $\Gamma_K^{2\to1}$) between different scales are very small in the balance of $K^1$. These results suggest that the intraseasonal KE in the deep SCS is primarily from the upper layer through pressure work and is finally damped by dissipation $F_K^1$. With respect to the $A^1$ budget in the deep SCS, a balance predominantly exists between the APE advection $\Delta_h Q_A^1$ and diffusion $F_A^1$. In contrast, local processes play a secondary role in the budget. The baroclinic transfer $\Gamma_A^{0\to1}$ extracts the APE from the background flow, which is mostly converted to the KE of intraseasonal fluctuations through a negative $b^1$.

This energy pathway is consistent with the observational and theoretical studies by de La Lama et al. (2016) and LaCasce (2017), who found that the QG flow over sloping topography is intensively surface-intensified and shielded from bottom friction, such that energy must be passed to TRWs to be dissipated. LaCasce et al. (2019) further demonstrated that the energy transfer due to baroclinic instability is effectively suppressed by the sloping topography and the deep flow is dominantly forced by interfacial motions related to surface eddies (i.e., through pressure work).

## 5. Summary and discussion

Based on the observations and HYCOM reanalysis, the characteristics and energetics of intraseasonal fluctuations in the abyssal SCS are investigated using the MS-EVA method. The results indicate substantial geographical variations in the deep energy reservoir on intraseasonal timescale. Several high-energy zones are found in the northwest of the Luzon Strait, northern slopes, DWBC region, and southwestern cyclonic gyre region. These energetic intraseasonal fluctuations are suggested to account for over 40% of the total energy variability over the steep topography, and the ratio can reach approximately 70% in the hot spots mentioned above, implying an active role in modulating the deep circulation in the SCS.

The normalized vorticity and divergence patterns suggest that the intraseasonal fluctuations in the abyssal SCS are characterized by QG dynamics, which are weakly divergent in most regions except for the slopes south of the Dongsha Islands, northwest of the Zhongsha Islands, and in the southwestern basin. The zonal wavenumber–frequency spectral analysis indicates that these fluctuations, in general, conform to the dispersion relations of TRWs and PRWs with periods of 5–90 days and wavelengths longer than 100 km.

In contrast to the upper layer, the intraseasonal fluctuations in the deep SCS exhibit a negative skewness of relative vorticity, which probably arises from the bottom drag due to flow–topography interactions. By examining the criteria of instabilities, the lateral shear of the intraseasonal motions in the deep SCS is too weak to cause centrifugal instability. This may account for the negative skewness of the relative vorticity due to the absence of centrifugal instability to suppress the exceptional negative vorticity. In contrast, the flow field with the frontogenetic strain enhances the horizontal buoyancy gradient to trigger the symmetric instability in the abyssal SCS.

Maps of intraseasonal energetics in the deep SCS exhibit a substantial geographic inhomogeneity that is closely associated with space-dependent dynamic differences. Pressure work plays a central role in regulating the energy reservoir, particularly over sloping topography. In contrast, cross-scale transfer due to the instability of background flow is weak in the deep SCS and mostly occurs in the lower portion of the northern slopes and the separation zone of the DWBC in the southwest. In these regions, the energy transport is active in carrying the energy away from a forward cascade to support an inverse cascade downstream. The implicit processes ($F_K^1$ and $F_A^1$), which appear to be related to the flow instability and get enhanced over the slopes, largely offset the pressure work in the energy balance.

Based on the basin-integrated budget of mechanical energy (ME; ME = KE + APE), Fig. 11 illustrates an intraseasonal energy pathway in the SCS. Note that the water column is roughly separated into two layers by 2000 m instead of the traditional three layers, which correspond to the climatological sandwich structure of the SCS circulation (e.g., Zhu et al., 2019), because the SCS has been observed to be vertically coupled as a two-layer dynamic system on the intraseasonal scale (e.g., Zhang et al., 2013; Shu et al., 2016; Wang et al., 2019; Zheng et al., 2021). In the upper layer, approximately 60% of the wind energy input to the large-scale circulation is suggested to be released by the generation of mesoscale eddies through baroclinic instability (Yang et al., 2013). The resulting EKE in the upper layer provides a primary source of intraseasonal fluctuations in the abyssal SCS through pressure work $\Delta Q_P^1$, which accounts for 79% of the total energy sources. For the rest, advective transport $\Delta Q_{K+A}^1$ and cross-scale transfer $\Gamma_{K+A}^{0\to 1}$ contribute to 18% and 3%, respectively. To reach equilibrium, the energy is damped mostly by dissipation $F_{K+A}^1$ (99% of the sinks). Our results highlight the universal dynamics that the net dissipation of energy in the deep ocean is largely supplied through pressure work across layers (Wunsch & Ferrari, 2004), which is consistent with the findings in the open ocean (Zhai & Marshall, 2013; Chen et al., 2014) and marginal seas (Yang et al., 2020; Maslo et al., 2020).

Our study attempts to depict a dynamic panorama of intraseasonal fluctuations that dominate the deep flow variability in the SCS. However, the resolution of the present model is too limited to resolve the energetic submesoscale processes in this region (e.g., Lin et al., 2020; Zhang et al., 2020). This would underestimate the forward cascade to smaller scales in the energy budget, which has been suggested to constitute the primary dissipation mechanism for mesoscale motions in the SCS (e.g., Zhang et al., 2016). In addition, the definition of APE used here is under the QG approximation and takes a quadratic form, which could be problematic in studying the submesoscale processes (e.g., Yang et al., 2021). For arbitrary stratifications, a more general nonquadratic APE definition (e.g., Holliday & McIntyre, 1981) should be taken into account. Observations and fine-resolution models are required in the future to obtain the full spectra and advance our understanding of the characteristics and energetics of the intraseasonal fluctuations and their roles in the energy cycle of the abyssal SCS. Also note that the analysis here is conducted in the $z$-coordinate, which should be less meaningful in dynamics than that in the isopycnic framework (e.g., Zhu et al., 2017). Nevertheless, how to derive the formulae of MS-EVA in the isopycnal coordinate remains a mathematical challenge that is left for our future study.

## Declaration of Competing Interest

The authors declare that they have no known competing financial interests or personal relationships that could have appeared to influence the work reported in this paper.

## Acknowledgements

This study is supported by the National Natural Science Foundation of China [42006007; 41906016; 42006009; 41806023], the China Postdoctoral Science Foundation [2020M682767], the Science and Technology Development Fund, Macau SAR [SKL-IOTSC-2021-2023], the Zhejiang Provincial Natural Science Foundation of China [LY21D060001], the Southern Marine Science and Engineering Guangdong Laboratory (Zhuhai) [SML2021SP207], the Shanghai Typhoon Fund [TFJJ202111], and the Zhejiang Provincial Key Research and Development Project [2021C03186]. The mooring data are available at https://doi.org/10.6084/m9.figshare.17696006.v1. The HYCOM data can be accessed from https://www.hycom.org/dataserver/gofs-3pt1/analysis. We are grateful to the anonymous reviewers for their insightful comments, and Drs. Shantong Sun and Yukun Qian for discussions to improve this paper.

## Appendix A. Pressure work in a two-layer model

In the light of Liang (2016), the pressure work on window $\varpi$ can be written as:

$$\Delta Q_P^{\varpi} = -\nabla\cdot\left(\frac{1}{\rho_0}\widehat{\mathbf{v}}^{\sim\varpi}\widehat{P}^{\sim\varpi}\right) = -\frac{1}{\rho_0}\widehat{\mathbf{v}}_h^{\sim\varpi}\cdot\nabla_h\widehat{P}^{\sim\varpi} + \frac{g}{\rho_0}\widehat{\rho}^{\sim\varpi}\widehat{w}^{\sim\varpi} \tag{A.1}$$

To better demonstrate how the pressure work functions, we use a two-layer model for illustration (Fig. A.1). In this simplified situation, Eq. (A.1) is integrated in each layer and approximately represented as:

$$\Delta Q_{P1}^{\varpi} \approx -\frac{gh_1}{\rho_0}\widehat{\mathbf{v}}_1^{\sim\varpi}\cdot\nabla\widehat{\eta}_1^{\sim\varpi} + \frac{g\widehat{\rho}_1^{\sim\varpi}h_1}{2\rho_0}\left(\widehat{w}_1^{\sim\varpi} + \widehat{w}_2^{\sim\omega}\right), \text{ and} \tag{A.2}$$

$$\Delta Q_{P2}^{\varpi} \approx -\frac{h_2}{\rho_0}\widehat{\mathbf{v}}_2^{\sim\varpi}\cdot\left[g\nabla\widehat{\eta}_1^{\sim\varpi} + g^{'}\nabla\widehat{\eta}_2^{\sim\varpi}\right] + \frac{g\widehat{\rho}_2^{\sim\varpi}h_2}{2\rho_0}\widehat{w}_2^{\sim\omega} \tag{A.3}$$

where $h_i$ is the layer thickness (positive) with the subscript $i$ being the layer index; $\eta_i = \sum_i^2 h_i + H$ is the surface/interface elevation with $H$ being the static water depth (negative); $\mathbf{v}_i$ is the horizontal velocity; $w_i$ is the vertical velocity of the surface/interface elevation; $\rho_i$ is the density; $g^{'} = g(\rho_2 - \rho_1)/\rho_0$ is the reduced gravitational acceleration.

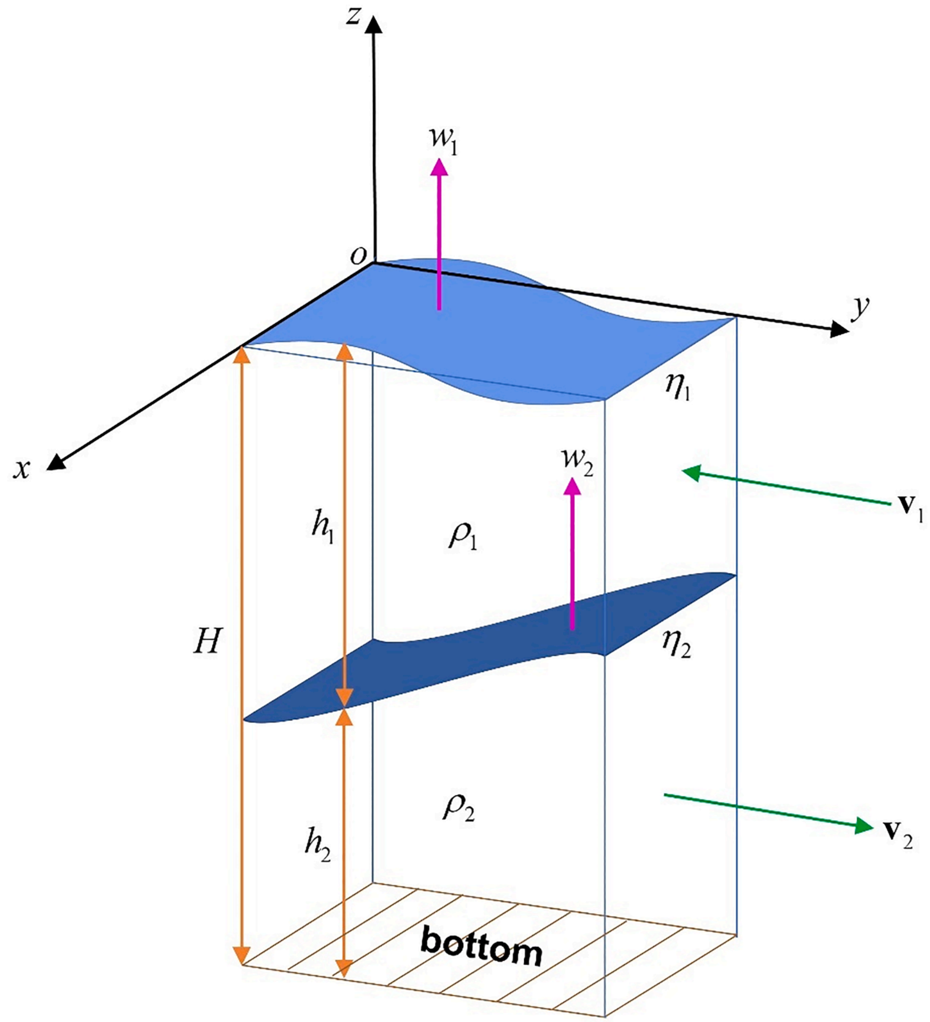

**Fig. A1.** Two-layer model used for demonstrating how the pressure work functions.

The first term on the right-hand side of Eqs. (A.2) and (A.3) denotes the work done by interface form stress and the second term represents the buoyancy conversion, both of which are closely related to the tilted isopycnal (reflected by the gradient of $\eta_i$ and the corresponding vertical motion $w_i$). These equations suggest that perturbation occurring in any layer is able to radiate energy throughout the water column if it could significantly deform the isopycnal to modulate the pressure field and change the center of mass. Hence, as mentioned in the introduction, the abyssal fluctuations in the SCS can be energized by the deep Luzon overflow or the surface eddies. To locate the major energy source, one can quantify the horizontal and vertical components of pressure work, as shown in Yang et al. (2020).

Moreover, according to Maslo et al. (2020), the vertical pressure work integrated in the upper and lower layers can offset each other as:

$$\iiint_{V_1} \frac{\partial}{\partial z}\left(-\frac{1}{\rho_0}\widehat{w}^{\sim\varpi}\widehat{P}^{\sim\varpi}\right)dV + \iiint_{V_2} \frac{\partial}{\partial z}\left(-\frac{1}{\rho_0}\widehat{w}^{\sim\varpi}\widehat{P}^{\sim\varpi}\right)dV \approx 0 \tag{A.4}$$

where $V_i$ is the control volume of each layer. Eq. (A.4) indicates that the divergence of the vertical pressure flux in the upper volume must lead to the convergence of vertical pressure flux in the lower volume and vice versa. This determines the intensity and direction of the energy exchange between layers, which is the key energetics underlying the well-known PV conservation. The detailed process analysis can be found in Quan et al. (2021a) and the relevant application to the linkage between the Kuroshio intrusion and the TRWs in the deep SCS can be referred to Quan et al. (2021b).

## References

Buckingham, C.E., Lucas, N.S., Belcher, S.E., Rippeth, T.P., Grant, A.L.M., Le Sommer, J., Ajayi, A.O., Naveira Garabato, A.C., 2019. The contribution of surface and submesoscale processes to turbulence in the open ocean surface boundary layer. J. Adv. Model. Earth Syst. 11 (12), 4066–4094. https://doi.org/10.1029/2019MS001801.

Capet, X., McWilliams, J.C., Molemaker, M.J., Shchepetkin, A.F., 2008. Mesoscale to submesoscale transition in the California Current system. Part II: Frontal processes. J. Phys. Oceanogr. 38, 44–64. https://doi.org/10.1175/2007JPO3672.1.

Chen, R., Flierl, G., Wunsch, C., 2014. A description of local and nonlocal eddy-mean flow interaction in a global eddy-permitting state estimate. J. Phys. Oceanogr. 44, 2336–2352. https://doi.org/10.1175/JPO-D-14-0009.1.

Cummings, J.A., 2005. Operational multivariate ocean data assimilation. Quart. J. Roy. Meteor. Soc. 131 (613), 3583–3604. https://doi.org/10.1256/qj.05.105.

Cummings, J.A., Smedstad, O.M., 2013. Variational data assimilation for the global ocean. Data Assimilation for Atmospheric, Oceanic and Hydrologic Applications, Vol. II, Springer, 303–343.

de La Lama, M.S., LaCasce, J.H., Fuhr, H.K., 2016. The vertical structure of ocean eddies. Dyn. Stat. Climate Syst. 1, dzw001. https://doi.org/10.1093/climsys/dzw001.

Dewar, W.K., McWilliams, J.C., Molermakser, M.J., 2015. Centrifugal instability and mixing in the California Undercurrent. J. Phys. Oceanogr. 45, 1224–1241. https://doi.org/10.1175/JPO-D-13-0269.1.

Dong, J., Fox-Kemper, B., Zhang, H., Dong, C., 2021. The scale and activity of symmetric instability estimated from a global submesoscale-permitting ocean model. J. Phys. Oceanogr. 51, 1655–1670. https://doi.org/10.1175/JPO-D-20-0159.1.

Donohue, K.A., Watts, D.R., Hamilton, P., Leben, R., Kennelly, M., 2016. Loop Current eddy formation and baroclinic instability. Dyn. Atmos. Oceans 76, 195–216. https://doi.org/10.1016/j.dynatmoce.2016.01.004.

Farrar, J.T., 2008. Observations of the dispersion characteristics and meridional sea level structure of equatorial waves in the Pacific Ocean. J. Phys. Oceanogr. 38, 1669–1689. https://doi.org/10.1175/2007JPO3890.1.

Ferrari, R., Wunsch, C., 2009. Ocean circulation kinetic energy: Reservoirs, sources, and sinks. Annu. Rev. Fluid Mech. 41 (1), 253–282. https://doi.org/10.1146/annurev.fluid.40.111406.102139.

Gula, J., Molemaker, M.J., McWilliams, J.C., 2016. Topographic generation of submesoscale centrifugal instability and energy dissipation. Nat. Commun. 7, 12811. https://doi.org/10.1038/ncomms12811.

Hamilton, P., 1990. Deep currents in the Gulf of Mexico. J. Phys. Oceanogr. 20, 1087–1104. https://doi.org/10.1175/1520-0485(1990)020<1087:DCITGO>2.0.CO;2.

Hamilton, P., 2007. Deep-current variability near the Sigsbee Escarpment in the Gulf of Mexico. J. Phys. Oceanogr. 37, 708–726. https://doi.org/10.1175/JPO2998.1.

Hamilton, P., 2009. Topographic Rossby waves in the Gulf of Mexico. Prog. Oceanogr. 82 (1), 1–31. https://doi.org/10.1016/j.pocean.2009.04.019.

Hamilton, P., Bower, A., Furey, H., Leben, R., Pérez-Brunius, P., 2019. The Loop Current: Observations of deep eddies and topographic waves. J. Phys. Oceanogr. 49, 1463–1483. https://doi.org/10.1175/JPO-D-18-0213.1.

Hogg, N.G., 1981. Topographic waves along 70°W on the continental rise. J. Mar. Res. 39, 627–649.

Hogg, N.G., 2000. Low-frequency variability on the western flanks of the Grand Banks. J. Mar. Res. 58, 523–545. https://doi.org/10.1357/002224000321511007.

Holliday, D., McIntyre, M.E., 1981. On potential energy density in an incompressible, stratified fluid. J. Fluid Mech. 107, 221–225. https://doi.org/10.1017/S0022112081001742.

Hoskins, B.J., 1974. The role of potential vorticity in symmetric stability and instability. Q. J. R. Meteorol. Soc. 100 (425), 480–482. https://doi.org/10.1002/qj.49710042520.

Johns, W.E., Watts, D.R., 1986. Time scales and structure of topographic Rossby waves and meanders in the deep Gulf Stream. J. Mar. Res. 44 (2), 267–290. https://doi.org/10.1357/002224086788405356.

Kang, D., Curchitser, E.N., 2015. Energetics of eddy-mean flow interactions in the Gulf Stream Region. J. Phys. Oceanogr. 45, 1103–1120. https://doi.org/10.1175/JPO-D-14-0200.1.

Klein, P., Hua, B.L., Lapeyre, G., Capet, X., Gentil, S.L., Sasaki, H., 2008. Upper ocean turbulence from high-resolution 3D simulations. J. Phys. Oceanogr. 38, 1748–1763. https://doi.org/10.1175/2007JPO3773.1.

LaCasce, J.H., 1998. A geostrophic vortex over a slope. J. Phys. Oceanogr. 28, 2362–2381. https://doi.org/10.1175/1520-0485(1998)028<2362:AGVOAS>2.0.CO;2.

LaCasce, J.H., 2017. The prevalence of oceanic surface modes. Geophys. Res. Lett. 44, 11097–11105. https://doi.org/10.1002/2017GL075430.

LaCasce, J.H., Escartin, J., Chassignet, E.P., Xu, X., 2019. Jet instability over smooth, corrugated, and realistic bathymetry. J. Phys. Oceanogr. 49, 585–605. https://doi.org/10.1175/JPO-D-18-0129.1.

Lan, J., Zhang, N., Wang, Y., 2013. On the dynamics of the South China Sea deep circulation. J. Geophys. Res.-Oceans 118 (3), 1206–1210. https://doi.org/10.1002/jgrc.20104.

Liang, X.S., 2016. Canonical transfer and multiscale energetics for primitive and quasigeostrophic atmospheres. J. Atmos. Sci. 73, 4439–4468. https://doi.org/10.1175/JAS-D-16-0131.1.

Liang, X.S., Robinson, A.R., 2005. Localized multiscale energy and vorticity analysis: I. Fundamentals. Dyn. Atmos. Oceans 38 (3–4), 195–230.

Liang, X.S., Robinson, A.R., 2007. Localized multi-scale energy and vorticity analysis: II. Finite-amplitude instability theory and validation. Dyn. Atmos. Oceans 44 (2), 51–76.

Liang, X.S., Anderson, D.G.M., 2007. Multiscale Window Transform. Multiscale Model. Simul. 6 (2), 437–467. https://doi.org/10.1137/06066895X.

Liang, X.S., Robinson, A.R., 2009. Multiscale processes and nonlinear dynamics of the circulation and upwelling events off Monterey Bay. J. Phys. Oceanogr. 39, 290–313. https://doi.org/10.1175/2008JPO3950.1.

Lin, H., Liu, Z., Hu, J., Menemenlis, D., Huang, Y., 2020. Characterizing meso- to submesoscale features in the South China Sea. Prog. Oceanogr. 188, 102420. https://doi.org/10.1016/j.pocean.2020.102420.

Lorenz, E.N., 1955. Available potential energy and the maintenance of the general circulation. Tellus 7 (2), 157–167.

Ma, J., Liang, X., 2017. Multiscale dynamical processes underlying the wintertime Atlantic blockings. J. Atmos. Sci. 74, 3815–3831. https://doi.org/10.1175/JAS-D-16-0295.1.

Ma, Q., Wang, F., Wang, J., Lyu, Y., 2019. Intensified deep ocean variability induced by topographic Rossby waves at the Pacific Yap-Mariana Junction. J. Geophys. Res.-Oceans 124 (11), 8360–8374. https://doi.org/10.1029/2019JC015490.

Maslo, A., De Souza, J.M.A.C., Pardo, J.S., 2020. Energetics of the deep Gulf of Mexico. J. Phys. Oceanogr. 50, 1655–1675. https://doi.org/10.1175/JPO-D-19-0308.1.

McWilliams, J.C., 2011. Fundamentals of geophysical fluid dynamics. Cambridge University Press 91–94.

McWilliams, J.C., 2016. Submesoscale currents in the ocean. Proc. R. Soc. A 472 (2189), 20160117. https://doi.org/10.1098/rspa.2016.0117.

Mensa, J.A., Garraffo, Z., Griffa, A., Özgökmen, T.M., Haza, A., Veneziani, M., 2013. Seasonality of the submesoscale dynamics in the Gulf Stream region. Ocean Dyn. 63 (8), 923–941. https://doi.org/10.1007/s10236-013-0633-1.

Molemaker, M.J., McWilliams, J.C., Capet, X., 2010. Balanced and unbalanced routes to dissipation in an equilibrated Eady flow. J. Fluid Mech. 654, 35–63. https://doi.org/10.1017/S0022112009993272.

Molemaker, M.J., McWilliams, J.C., Dewar, W.K., 2015. Submesoscale instability and generation of mesoscale anticyclones near a separation of the California Undercurrent. J. Phys. Oceanogr. 45, 613–629. https://doi.org/10.1175/JPO-D-13-0225.1.

Morey, S.L., Gopalakrishnan, G., Sanz, E.P., Azevedo Correia De Souza, J.M., Donohue, K., Pérez-Brunius, P., Dukhovskoy, D., Chassignet, E., Cornuelle, B., Bower, A., Furey, H., Hamilton, P., Candela, J., 2020. Assessment of numerical simulations of deep circulation and variability in the Gulf of Mexico using recent observations. J. Phys. Oceanogr. 50 (4), 1045–1064. https://doi.org/10.1175/JPO-D-19-0137.1.

Oey, L.Y., 2008. Loop Current and deep eddies. J. Phys. Oceanogr. 38, 1426–1449. https://doi.org/10.1175/2007JPO3818.1.

Oey, L.Y., Lee, H.C., 2002. Deep eddy energy and topographic Rossby waves in the Gulf of Mexico. J. Phys. Oceanogr. 32, 3499–3527. https://doi.org/10.1175/1520-0485(2002)032<3499:DEEATR>2.0.CO;2.

Pedlosky, J., 1987. Geophysical Fluid Dynamics, 2nd ed. Springer-Verlag, p. 710.

Peña-Molino, B., Joyce, T.M., Toole, J.M., 2012. Variability in the deep western boundary current: Local versus remote forcing. J. Geophys. Res. 117, C12022 https://doi.org/10.1029/2012JC008369.

Pickart, R.S., 1995. Gulf Stream-generated topographic Rossby waves. J. Phys. Oceanogr. 25, 574–586. https://doi.org/10.1175/1520-0485(1995)025<0574:GSTRW>2.0.CO;2.

Pickart, R.S., Watts, D.R., 1990. Deep western boundary current variability at Cape Hatteras. J. Mar. Res. 48 (4), 765–791. https://doi.org/10.1357/002224090784988674.

Quan, Q., Xue, H., 2018. Layered model and insights into the vertical coupling of the South China Sea circulation in the upper and middle layers. Ocean Model. 129, 75–92. https://doi.org/10.1016/j.ocemod.2018.06.006.

Quan, Q., Xue, H., 2019. Influence of abyssal mixing on the multilayer circulation in the South China Sea. J. Phys. Oceanogr. 49, 3045–3060. https://doi.org/10.1175/JPO-D-19-0020.1.

Quan, Q., Cai, Z., Jin, G., Liu, Z., 2021a. Topographic Rossby waves in the abyssal South China Sea. J. Phys. Oceanogr. 51, 1795–1812. https://doi.org/10.1175/JPO-D-20-0187.1.

Quan, Q., Liu, Z., Sun, S., Cai, Z., Yang, Y., Jin, G., Li, Z., Liang, X.S., 2021b. Influence of the Kuroshio intrusion on deep flow intraseasonal variability in the northern South China Sea. J. Geophys. Res.-Oceans 126, e2021JC017429. https://doi.org/10.1029/2021JC017429.

Rhines, P., 1970. Edge-, bottom-, and Rossby waves in a rotating stratified fluid. Geophys. Fluid Dyn. 1 (3-4), 273–302. https://doi.org/10.1080/03091927009365776.

Shu, Y., Xue, H., Wang, D., Chai, F., Xie, Q., Yao, J., Xiao, J., 2014. Meridional overturning circulation in the South China Sea envisioned from the high-resolution global reanalysis data GLBa0.08. J. Geophys. Res.-Oceans 119 (5), 3012–3028. https://doi.org/10.1002/2013JC009583.

Shu, Y., Xue, H., Wang, D., Chai, F., Xie, Q., Cai, S., Chen, R., Chen, J., Li, J., He, Y., 2016. Persistent and energetic bottom-trapped topographic Rossby waves observed in the southern South China Sea. Sci. Rep. 6, 24338. https://doi.org/10.1038/srep24338.

Siegelman, L., 2020. Energetic submesoscale dynamics in the ocean interior. J. Phys. Oceanogr. 50, 727–749. https://doi.org/10.1175/JPO-D-19-0253.1.

Sun, Z., Zhang, Z., Qiu, B., Zhang, X., Zhou, C., Huang, X., Zhao, W., Tian, J., 2020. Three-dimensional structure and interannual variability of the Kuroshio loop current in the northeastern South China Sea. J. Phys. Oceanogr. 50, 2437–2455. https://doi.org/10.1175/JPO-D-20-0058.1.

Taylor, J.R., Ferrari, R., 2009. On the equilibration of a symmetrically unstable front via a secondary shear instability. J. Fluid Mech. 622, 103–113. https://doi.org/10.1017/S0022112008005272.

Thomas, L.N., Taylor, J.R., Ferrari, R., Joyce, T.M., 2013. Symmetric instability in the Gulf Stream. Deep-Sea Res. II 91, 96–110. https://doi.org/10.1016/j.dsr2.2013.02.025.

Thompson, R.O.R.Y., 1977. Observations of Rossby waves near site D. Prog. Oceanogr. 7, 135–162. https://doi.org/10.1016/0079-6611(77)90003-9.

Thompson, R.O.R.Y., Luyten, J.R., 1976. Evidence for bottom-trapped topographic Rossby waves from single moorings. Deep Sea Res. 23 (7), 629–635. https://doi.org/10.1016/0011-7471(76)90005-X.

Tian, J., Yang, Q., Zhao, W., 2009. Enhanced diapycnal mixing in the South China Sea. J. Phys. Oceanogr. 39, 3191–3203. https://doi.org/10.1175/2009JPO3899.1.

Von Storch, J.-S., Eden, C., Fast, I., Haak, H., Hernandez-Deckers, D., Maier-Reimer, E., Marotzke, J., Stammer, D., 2012. An estimate of the Lorenz energy cycle for the world ocean based on the STORM/NCEP simulation. J. Phys. Oceanogr. 42, 2185–2205. https://doi.org/10.1175/JPO-D-12-079.1.

Wang, D., Xiao, J., Shu, Y., Xie, Q., Chen, J., Wang, Q., 2016a. Progress on deep circulation and meridional overturning circulation in the South China Sea. Sci. Chin 59, 1827–1833. https://doi.org/10.1007/s11430-016-5324-6.

Wang, G., Xie, S., Qu, T., Huang, R., 2011. Deep South China Sea circulation. Geophys. Res. Lett. 38, L05601. https://doi.org/10.1029/2010GL046626.

Wang, Q., Zeng, L., Shu, Y., Li, J., Chen, J., He, Y., Yao, J., Wang, D., Zhou, W., 2019. Energetic topographic Rossby waves in the northern South China Sea. J. Phys. Oceanogr. 49, 2697–2714. https://doi.org/10.1175/JPO-D-18-0247.1.

Wang, Q., Zhou, W., Zeng, L., Chen, J., He, Y., Wang, D., 2020. Intraseasonal variability of cross-slope flow in the northern South China Sea. J. Phys. Oceanogr. 50, 2071–2084. https://doi.org/10.1175/JPO-D-19-0293.1.

Wang, X., Peng, S., Liu, Z., Huang, R., Qian, Y., Li, Y., 2016b. Tidal mixing in the South China Sea: An estimate based on the internal tide energetics. J. Phys. Oceanogr. 46, 107–124. https://doi.org/10.1175/JPO-D-15-0082.1.

Wunsch, C., Ferrari, R., 2004. Vertical mixing, energy, and the general circulation of the oceans. Annu. Rev. Fluid Mech. 36, 281–314. https://doi.org/10.1146/annurev.fluid.36.050802.12212.

Xu, F., Chang, Y.L., Oey, L.Y., Hamilton, P., 2013. Loop current growth and eddy shedding using models and observations: Analyses of the July 2011 eddy-shedding event. J. Phys. Oceanogr. 43, 1015–1027. https://doi.org/10.1175/JPO-D-12-0138.1.

Yan, Y., Wang, G., Xue, H., Chai, F., 2019. Buoyancy effect on the winter South China Sea western boundary current. J. Geophys. Res.-Oceans 124 (10), 6871–6885. https://doi.org/10.1029/2019JC015079.

Yang, H., Wu, L., Liu, H., Yu, Y., 2013. Eddy energy sources and sinks in the South China Sea. J. Geophys. Res.-Oceans 118 (9), 4716–4726. https://doi.org/10.1002/jgrc.20343.

Yang, Y., Liang, X.S., 2016. The instabilities and multiscale energetics underlying the mean-interannual-eddy interactions in the Kuroshio extension region. J. Phys. Oceanogr. 46, 1477–1494. https://doi.org/10.1175/JPO-D-15-0226.1.

Yang, Y., Liang, X.S., 2018. On the seasonal eddy variability in the Kuroshio extension. J. Phys. Oceanogr. 48, 1675–1689. https://doi.org/10.1175/JPO-D-18-0058.1.

Yang, Y., Liang, X.S., Qiu, B., Chen, S., 2017. On the decadal variability of the eddy kinetic energy in the Kuroshio extension. J. Phys. Oceanogr. 47, 1169–1187. https://doi.org/10.1175/JPO-D-16-0201.1.

Yang, Y., Weisberg, R.H., Liu, Y., Liang, X.S., 2020. Instabilities and multiscale interactions underlying the Loop Current eddy shedding in the Gulf of Mexico. J. Phys. Oceanogr. 50, 1289–1317. https://doi.org/10.1175/JPO-D-19-0202.1.

Yang, Y., McWilliams, J.C., Liang, X.S., Zhang, H., Weisberg, R.H., Liu, Y., Menemenlis, D., 2021. Spatial and temporal characteristics of the submesoscale energetics in the Gulf of Mexico. J. Phys. Oceanogr. 51, 475–489. https://doi.org/10.1175/JPO-D-20-0247.1.

Zhai, X., Marshall, D.P., 2013. Vertical eddy energy fluxes in the North Atlantic subtropical and subpolar gyres. J. Phys. Oceanogr. 43, 95–103. https://doi.org/10.1175/JPO-D-12-021.1.

Zhang, Z., Zhao, W., Tian, J., Liang, X., 2013. A mesoscale eddy pair southwest of Taiwan and its influence on deep circulation. J. Geophys. Res.-Oceans 118 (12), 6479–6494. https://doi.org/10.1002/2013JC008994.

Zhang, Z., Tian, J., Qiu, B., Zhao, W., Chang, P., Wu, D., Wan, X., 2016. Observed 3D structure, generation, and dissipation of oceanic mesoscale eddies in the South China Sea. Sci. Rep. 6, 24349. https://doi.org/10.1038/srep24349.

Zhang, Z., Zhao, W., Qiu, B., Tian, J., 2017. Anticyclonic eddy sheddings from Kuroshio Loop and the accompanying cyclonic eddy in the northeastern South China Sea. J. Phys. Oceanogr. 47, 1243–1259. https://doi.org/10.1175/JPO-D-16-0185.1.

Zhang, Z., Zhang, Y., Qiu, B., Sasaki, H., Sun, Z., Zhang, X., Zhao, W., Tian, J., 2020. Spatiotemporal characteristics and generation mechanisms of submesoscale currents in the northeastern South China Sea revealed by numerical simulations. J. Geophys. Res.-Oceans 125, e2019JC015404. https://doi.org/10.1029/2019JC015404.

Zhao, B., Timmermans, M.-L., 2018. Topographic Rossby waves in the Arctic Ocean's Beaufort Gyre. J. Geophys. Res.-Oceans 123 (9), 6521–6530. https://doi.org/10.1029/2018JC014233.

Zheng, H., Zhu, X., Zhang, C., Zhao, R., Zhu, Z., Liu, Z., 2021. Propagation of topographic Rossby waves in the deep basin of the South China Sea based on abyssal current observations. J. Phys. Oceanogr. 51, 2783–2791. https://doi.org/10.1175/JPO-D-21-0051.1.

Zhong, Y., Bracco, A., 2013. Submesoscale impacts on horizontal and vertical transport in the Gulf of Mexico. J. Geophys. Res.-Oceans 118 (10), 5651–5668. https://doi.org/10.1002/jgrc.20402.

Zhou, C., Zhao, W., Tian, J., Zhao, X., Zhu, Y., Yang, Q., Qu, T., 2017. Deep western boundary current in the South China Sea. Sci. Rep. 7, 9303. https://doi.org/10.1038/s41598-017-09436-2.

Zhou, M., Wang, G., Liu, W., Chen, C., 2020. Variability of the observed deep western boundary current in the South China Sea. J. Phys. Oceanogr. 50, 2953–2963. https://doi.org/10.1175/JPO-D-20-0013.1.

Zhu, Y., Sun, J., Wang, Y., Wei, Z., Yang, D., Qu, T., 2017. Effect of potential vorticity flux on the circulation in the South China Sea. J. Geophys. Res.-Oceans 122 (8), 6454–6469. https://doi.org/10.1002/2016JC012375.

Zhu, Y., Sun, J., Wang, Y., Li, S., Xu, T., Wei, Z., Qu, T., 2019. Overview of the multi-layer circulation in the South China Sea. Prog. Oceanogr. 175, 171–182. https://doi.org/10.1016/j.pocean.2019.04.001.